Monthly Notices of the ROYAL ASTRONOMICAL SOCIETY

MNRAS **530,** 2315–2335 (2024)
Advance Access publication 2024 April 13

https://doi.org/10.1093/mnras/stae1010

Strong outflows and inefficient star formation in the reionization-era ultrafaint dwarf galaxy Eridanus II

Nathan R. Sandford [1,2★] David H. Weinberg,[3] Daniel R. Weisz [1] and Sal Wanying Fu[1]

[1]*Department of Astronomy, University of California Berkeley, Berkeley, CA 94720, USA*
[2]*Department of Astronomy and Astrophysics, University of Toronto, 50 St. George Street, Toronto, ON M5P 0A2, Canada*
[3]*Department of Astronomy and Center for Cosmology and AstroParticle Physics, The Ohio State University, Columbus, OH 43210, USA*

Accepted 2024 April 10. Received 2024 April 10; in original form 2023 August 31

ABSTRACT

We present novel constraints on the underlying galaxy formation physics (e.g. mass-loading factor, star formation history, and metal retention) at $z \gtrsim 7$ for the low-mass ($M_* \sim 10^5$ M$_\odot$) Local Group ultrafaint dwarf galaxy (UFD) Eridanus II (Eri II). Using a hierarchical Bayesian framework, we apply a one-zone chemical evolution model to Eri II's CaHK-based photometric metallicity distribution function (MDF; [Fe/H]) and find that the evolution of Eri II is well characterized by a short, exponentially declining star formation history ($\tau_{\rm SFH} = 0.39\pm^{0.18}_{0.13}$ Gyr), a low star formation efficiency ($\tau_{\rm SFE} = 27.56\pm^{25.14}_{12.92}$ Gyr), and a large mass-loading factor ($\eta = 194.53\pm^{33.37}_{42.67}$). Our results are consistent with Eri II forming the majority of its stars before the end of reionization. The large mass-loading factor implies strong outflows in the early history of Eri II and is in good agreement with theoretical predictions for the mass scaling of galactic winds. It also results in the ejection of >90 per cent of the metals produced in Eri II. We make predictions for the distribution of [Mg/Fe]–[Fe/H] in Eri II as well as the prevalence of ultra metal-poor stars, both of which can be tested by future chemical abundance measurements. Spectroscopic follow-up of the highest metallicity stars in Eri II ([Fe/H] > -2) will greatly improve model constraints. Our new framework can readily be applied to all UFDs throughout the Local Group, providing new insights into the underlying physics governing the evolution of the faintest galaxies in the reionization era.

Key words: galaxies: dwarf – galaxies: evolution – galaxies: stellar content.

1 INTRODUCTION

At the faintest end of the galaxy luminosity function, ultrafaint dwarf galaxies (UFDs) are some of the oldest ($\gtrsim$13 Gyr), lowest mass ($M_* \lesssim 10^6$ M$_\odot$), most metal-poor ([Fe/H] $\lesssim -2.0$), and dark-matter-dominated ($M/L \gtrsim 100$) systems in the Universe (e.g. Simon 2019, and references therein). As such, Local Group (LG) UFDs and their stellar populations provide a powerful lens through which to study a wide range of astrophysics from the nature of dark matter to star formation, stellar evolution, and chemical enrichment in the early Universe before the epoch of reionization.

Eridanus II (Eri II; $M_V = -7.1$), initially discovered in the Dark Energy Survey by Bechtol et al. (2015) and Koposov et al. (2015), is an ideal UFD to study low-mass galaxy evolution at early times. Its dynamical mass ($M_{1/2} = 1.2\pm^{0.4}_{0.3} \times 10^7$ M$_\odot$) and stellar metallicity distribution function (MDF; $\langle$[Fe/H]$\rangle = -2.38 \pm 0.13$ and $\sigma_{\rm [Fe/H]} = 0.47\pm^{0.12}_{0.09}$) measured from calcium triplet (CaT) observations of Eri II's brightest red giant branch (RGB) stars confirm its status as a metal-poor dark-matter-dominated dwarf galaxy (Li et al. 2017). Later spectroscopic and variable star studies provided independent confirmation of Eri II's metal-poor dark-matter-dominated nature (Zoutendijk et al. 2020; Martínez-Vázquez et al. 2021; Zoutendijk et al. 2021). Meanwhile, its star formation history (SFH) measured from deep broad-band imaging is consistent with Eri II forming nearly all of its stellar mass ($\sim 2 \times 10^5$ M$_\odot$) in a short (<500 Myr) burst over 13 Gyr ago, making it a true relic of the pre-reionization era (Gallart et al. 2021; Simon et al. 2021). Further, its current distance at ~350 kpc (Crnojević et al. 2016; Li et al. 2017; Martínez-Vázquez et al. 2021; Simon et al. 2021) and its orbit inferred from *Gaia* eDR3 proper motions place Eri II at first infall into the Milky Way (MW), indicating that it likely evolved in isolation and thus removing the need to account for ram pressure stripping or tidal interactions during its evolution (Battaglia et al. 2022; Fu et al. 2022).

Recently, Fu et al. (2022, hereafter F22) presented newly measured [Fe/H] abundances for 60 Eri II RGB stars from deep narrow-band photometry of the calcium H&K doublet (CaHK) acquired with the *Hubble Space Telescope* (*HST*). These observations roughly quadrupled the number of Eri II stars with known metallicities, substantially improving the sampling of Eri II's MDF measured from the CaT observations of Li et al. (2017). F22 found Eri II's MDF to be characterized by a mean metallicity of $\langle$[Fe/H]$\rangle = -2.50 \pm 0.07$ with a dispersion of $\sigma_{\rm [Fe/H]} = 0.42 \pm 0.06$. While F22 fit simple 'closed box' and 'leaky box' chemical evolution models to the Eri II MDF, constraints on the physical processes (e.g. star formation and outflows) governing the galaxy's chemical evolution have yet to be attempted.

★ E-mail: nathan.sandford@utoronto.ca

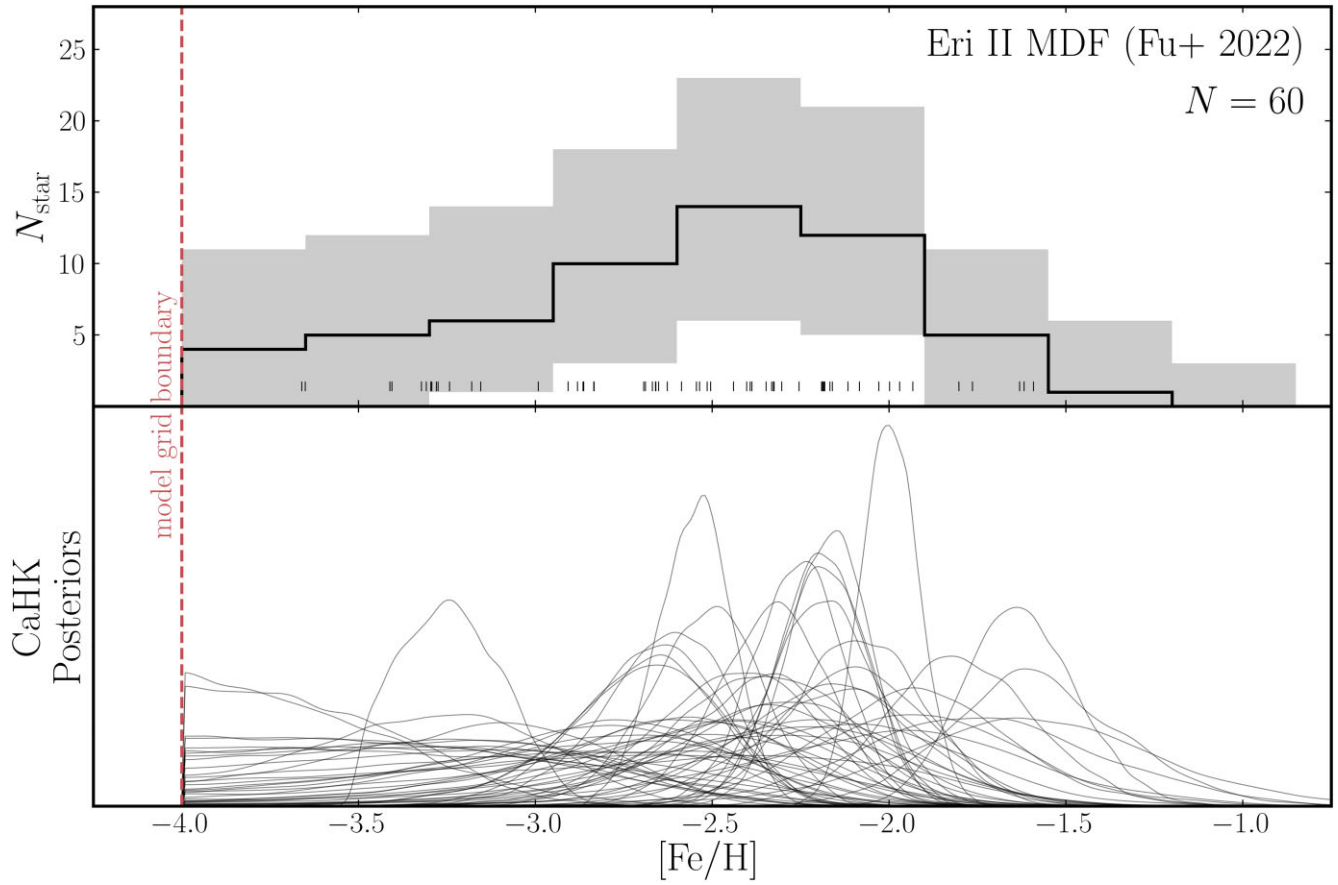

Figure 1. Top: distribution of narrow-band CaHK metallicity measurements for 60 RGB stars in the Eri II UFD reported by F22. The median measurement uncertainty (0.35 dex) is reflected in the choice of bin size. Each individual measurement is represented by a tick in the rug plot. Uncertainties on the observed MDF (grey-shaded regions) are estimated via bootstrapping (with replacement) from the F22 sample and drawing from each star's [Fe/H] posterior distribution. Bottom: posterior [Fe/H] distributions for each star approximated by applying bounded Gaussian KDE to the MCMC samples of F22. The posteriors of several stars exhibit long tails towards low metallicity and/or truncation at the limit of the MIST model grid ([Fe/H] = −4.0).

Here, we use the analytic one-zone galactic chemical evolution models first presented in Weinberg, Andrews & Freudenburg (2017, hereafter WAF17) to fit the MDF of Eri II in a hierarchical Bayesian framework that can be applied uniformly to the MDFs of all observed UFDs, present and future. The key assumption of these models is that the star-forming gas reservoir of Eri II is efficiently mixed and can therefore be approximated as chemically homogeneous at any given time. The models enable us to infer key galactic evolution parameters for Eri II, including the star formation efficiency (SFE), SFH time-scale, and the mass-loading factor for Eri II and place them in context of past observational and theoretical low-mass galaxy studies.

The structure of this paper is as follows. In Section 2, we summarize the data included in our analysis. In Section 3, we describe our chemical evolution model and fitting techniques. We present and discuss our results in Sections 4 and 5, respectively, before concluding in Section 6. Throughout this work when converting between redshift and age, we assume the flat lambda-cold dark matter cosmology of Planck Collaboration (2020).

2 DATA

In this study, we use the iron abundances, [Fe/H], of 60 stars in the UFD galaxy Eri II measured by F22 from *HST* CaHK narrow-band photometry in conjunction with archival *HST* broad-band photometry. This sample contains only RGB stars with $F475 \lesssim 24$ in the inner 260 pc region of Eri II and excludes all stars within 2 half-light radii, $r_{\rm h}$, of the galaxy's singular star cluster.

F22 fit the CaHK colour index,[1] of each star using 13 Gyr old mono-metallic α-enhanced Modules for Experiments in Sellar Atrophysics (MESA) Isochrones and Stellar Tracks (MIST) isochrones (Choi et al. 2016; Dotter 2016) to infer [Fe/H] for each star in their sample. Employing Bayesian techniques enabled them to recover the posterior distribution of [Fe/H] for each star, assuming a flat prior. Many stars in their sample exhibit non-Gaussian uncertainties in [Fe/H] with long tails towards low metallicity, which occur as a result of less distinguishable CaHK absorption features in metal-poor stars. A few stars have [Fe/H] posteriors that truncate at [Fe/H] = −4.0 due to the limited extent of the MIST model grid. To capture this non-Gaussianity in our analysis, we approximate the sampled posterior distribution of each star from the Markov chain Monte Carlo (MCMC) chains of F22 using bounded Gaussian kernel density estimation (KDE).

Fig. 1 shows the MDF of the 60 Eri II RGB stars in our sample. In the top panel, we plot the MDF as a histogram using the posterior median [Fe/H] values for each star reported by F22. A bin width of

[1]Defined as $F395N - F475W - 1.5(F475W - F814W)$.

Table 1. Fiducial model parameters adopted in this work. The implementation of these parameters is described in detail in WAF17. Priors for the free parameters are introduced in Section 3.2 and adopt the following notations for truncated normal and uniform distributions respectively: $X \sim \mathcal{TN}(\mu_X, \sigma_X, X_{\rm min}, X_{\rm max})$ and $X \sim \mathcal{U}(X_{\rm min}, X_{\rm max})$, where μ_X, σ_X, $X_{\rm min}$, and $X_{\rm max}$ are the mean, standard deviation, lower bound, and upper bound of the distribution. IMF-integrated yields represent the mass of an element produced per unit mass of star formation for a given nucleosynthetic channel. The SN Ia DTD is a sum of two exponentials that accurately approximates a $t^{-1.1}$ power law.

Parameter	Description	Value/priors	Units	References
	Fixed parameters			
Δt	Time-step	10^{-5}	Gyr	...
$Z_{\rm Fe,\odot}$	Solar iron abundance by mass	0.0013	...	[1]
$Z_{\rm Mg,\odot}$	Solar magnesium abundance by mass	0.0007	...	[1]
$y^{\rm cc}_{\rm Mg}$	IMF-integrated CCSN magnesium yield	0.001	...	[2]
$y^{\rm cc}_{\rm Fe}$	IMF-integrated CCSN iron yield	0.0006	...	[2]
$y^{\rm Ia}_{\rm Mg}$	IMF-integrated SN Ia magnesium yield	0.0	...	[2]
$y^{\rm Ia}_{\rm Fe}$	IMF-integrated SN Ia iron yield	0.0012	...	[2]
r	Mass recycling fraction	0.37	...	[3]
$\alpha_{\rm Ia}$	Slope of SN Ia power-law DTD	-1.1	...	[4]
t_D	Minimum delay time for SNe Ia	0.05	Gyr	[3]
$f_{\rm ret}$	Fraction of newly produced metals retained by the ISM	1.0	...	...
	Free parameters			
$\tau_{\rm SFH}$	Star formation history time-scale, $\dot{M}_* \propto e^{-t/\tau_{\rm SFH}}$	$\mathcal{TN}(0.7, 0.3, 0.0, \infty)$	Gyr	[5]
$\tau_{\rm SFE}$	$= M_g/\dot{M}_*$, star formation efficiency time-scale	$\mathcal{U}(0, 10^4)$	Gyr	...
$t_{\rm trunc}$	Time of SFH truncation	$\mathcal{TN}(1.0, 0.5, 0.0, \infty)$	Gyr	[5]
η	$= \dot{M}_{\rm outflow}/\dot{M}_*$, mass-loading factor	$\mathcal{U}(0, 10^3)$	...	..

Notes. References: [1] Asplund et al. (2009), [2] Conroy et al. (2022), [3] Weinberg et al. (2017), [4] Maoz, Mannucci & Brandt (2012), and [5] Gallart et al. (2021).

0.35 dex is chosen to match the median measurement uncertainty. In the bottom panel, we display the approximated CaHK [Fe/H] posterior distribution for each star. These will later be used as priors in our analysis (see Section 3.2).

3 METHODS

3.1 Chemical evolution model

We adopt the galactic chemical evolution framework presented and discussed extensively in WAF17. In brief, this analytic model tracks the time evolution of abundances in a fully mixed (one-zone) system experiencing gas accretion, star formation, supernova (SN) enrichment, and outflows. Relative to previous analytic models, the key innovation of the WAF17 model is its ability to separately track both rapid enrichment from core-collapse SNe (CCSNe) and delayed enrichment from Type Ia SNe (SNe Ia). In the limit of prompt enrichment and no gas accretion, the model approaches 'closed box' (no outflow) or 'leaky box' scenarios, but the behaviour in this limit is quite different from that of models with ongoing accretion. A complete description of the model and its input parameters can be found in WAF17 (see especially their table 1). We summarize parameter choices for our fiducial Eri II model below and in Table 1. We also consider several alternative models with variations on the fiducial choices, which we describe in Section 3.3. A discussion of key model assumptions and their potential impact on the interpretation of Eri II's chemical evolution is presented in Section 5.3.

3.1.1 Star formation

Motivated by the SFH measured for Eri II by Simon et al. (2021) and Gallart et al. (2021), we adopt a truncated exponentially declining star formation rate (SFR)

$$\dot{M}_* \propto \begin{cases} \exp\left(-t/\tau_{\rm SFH}\right), & \text{if } t \leq t_{\rm trunc} \\ 0, & \text{if } t > t_{\rm trunc}, \end{cases} \quad (1)$$

where $\tau_{\rm SFH}$ is the SFH time-scale and $t_{\rm trunc}$ is the time at which all star formation ceases. The sharp truncation of the SFH is adopted to simulate the abrupt quenching of low-mass galaxies (e.g. from ram pressure stripping or reionization). We leave both $\tau_{\rm SFH}$ and $t_{\rm trunc}$ as free parameters.

The conversion of gas into stars is governed by a linear star formation law characterized by the SFE time-scale (or inverse SFE) according to

$$\tau_{\rm SFE} \equiv {\rm SFE}^{-1} \equiv M_g/\dot{M}_*, \quad (2)$$

where M_g and $\dot{M}_*$ are the gas mass and SFR, respectively. We leave $\tau_{\rm SFE}$ as a free parameter. (In WAF17, the SFE time-scale is denoted τ_*.)

3.1.2 Gas flows

The mass recycling fraction, r, sets the fraction of mass formed into stars that is immediately returned to the ISM (interstellar medium) without further chemical enrichment by CCSNe and asymptotic giant branch (AGB) stars. Because this recycling is not a source of new metals, its main effect is to slow the rate at which metals in the ISM are depleted by star formation. We adopt a recycling fraction $r = 0.37$, which is appropriate for a Kroupa (2001) IMF (initial mass function) after 1 Gyr. As shown by WAF17, treating this recycling as instantaneous is an accurate approximation, because much of the recycled material originates from stars with short lifetimes (see their fig. 7). Moreover, the effect of this approximation is small when the metallicity is low or when galactic winds are important as is the case for Eri II.

Gas ejected from the ISM by stellar feedback (i.e. CCSNe and AGB winds) scales linearly with the SFR according to

$$\eta = \dot{M}_{\rm outflow}/\dot{M}_*, \quad (3)$$

where η is the mass-loading factor. We leave η as a free parameter.

Gas inflow is specified implicitly in the model through the provided SFH, SFE, mass recycling fraction, and mass-loading factor such that the depletion of gas by star formation and outflows is sufficiently balanced to maintain the SFR given in equation (1). WAF17 demonstrates that the gas infall rate can be obtained analytically in terms of other model parameters as

$$\dot{M}_{\rm inf} = (1 + \eta - r)\dot{M}_* + \tau_{\rm SFE}\ddot{M}_* \quad (4)$$

(see their equation 9). For our exponential SFH, $\ddot{M}_* = -\dot{M}_*/\tau_{\rm SFH}$. We assume accreted gas is pristine and free of previous enrichment.

3.1.3 Chemical enrichment

Enrichment from CCSNe is assumed to occur instantaneously following star formation. Enrichment from SNe Ia, on the other hand, is assumed to follow a delay time distribution (DTD) that accurately approximates the $t^{-1.1}$ power law found empirically by Maoz et al. (2012).[2] We adopt a minimum time delay, t_D, of 0.05 Gyr corresponding to the lifetime of the most massive white dwarf progenitors.

The WAF17 model parametrizes chemical enrichment using dimensionless IMF-weighted yield parameters, which are presumed to be independent of metallicity. These yield parameters represent the mass of elements produced per unit mass of star formation. We adopt lower yield values than WAF17, motivated by the recent study of Rodríguez, Maoz & Nakar (2023), who infer a population-averaged mean Fe yield of 0.058 $M_\odot$ per CCSN. A Kroupa (2001) IMF predicts approximately one $M > 8$ $M_\odot$ star per 100 $M_\odot$ of star formation, so this estimate suggests a dimensionless CC SN Fe yield $y^{\rm cc}_{\rm Fe} \approx 6 \times 10^{-4}$, which we adopt for our models. Although our data do not include Mg abundances, we present predictions of [Mg/Fe] versus [Fe/H] that could be tested with future data. We choose $y^{\rm cc}_{\rm Mg} = 0.001$, which puts the low-metallicity α 'plateau' at [Mg/Fe] ≈ 0.5, roughly consistent with measurements in the MW disc from the H3 Survey (Conroy et al. 2022). We assume that Mg has no SN Ia contribution, that is, $y^{\rm Ia}_{\rm Mg} = 0$. Finally, we choose $y^{\rm Ia}_{\rm Fe} = 0.0012$ so that models evolved with 'Milky Way disc' parameters similar to WAF17 reach [Mg/Fe] ≈ 0 at late times. For an Fe yield of 0.7 $M_\odot$ per SN Ia (e.g. Howell et al. 2009), this $y^{\rm Ia}_{\rm Fe}$ corresponds to 1.7×10^{-3} SNe Ia per $M_\odot$ of star formation, approximately consistent with the rate of 1.3×10^{-3} SNe Ia per $M_\odot$ found by Maoz & Graur (2017).

CC and SN Ia yields and their uncertainties are discussed at length by Weinberg et al. (2023), who develop empirically calibrated α-element and Fe yields building on the measurements of Rodríguez et al. (2023). Relative to their fiducial values, our adopted $y^{\rm cc}_{\rm Fe}$ is higher by ∼25 per cent, and our adopted $y^{\rm cc}_{\rm Mg}$ and $y^{\rm Ia}_{\rm Fe}$ are higher by ∼50 per cent, compared to the ∼25 per cent fractional uncertainty estimates of Weinberg et al. (2023). However, the empirical calibration of Weinberg et al. (2023), which is a more detailed form of the argument above, is dominated by stars near solar metallicity, and yields at much lower metallicity could differ (e.g. because of differences in black hole formation or the stellar IMF). Griffith et al. (2021) show that such changes can alter theoretically predicted CCSN yields by factors of 2–3, in addition to uncertainties associated with the SN models themselves. In chemical evolution models, there is a strong degeneracy between the overall scale of yields and the required level of outflows (see Weinberg et al. 2023 and appendix B of Johnson et al. 2023b). However, while factor of 2–3 changes to yields would produce comparable changes (of opposite direction) in our inferred η values, they would not alter our qualitative conclusion that strong outflows and inefficient star formation (high η and long $\tau_{\rm SFE}$) are required to explain the observed MDF of Eri II.

The products of CCSNe and SNe Ia that are deposited into the ISM are assumed to mix completely and instantaneously such that they are available for star formation immediately. This simplification, known as the instantaneous mixing approximation, has been shown to be a reasonable assumptions for CCSNe and SNe Ia products in low-mass, ancient galaxies like Eri II (e.g. Escala et al. 2018).

The WAF17 model assumes that outflows are comprised of gas at the ISM metallicity, so that the associated metal loss rate is $\eta \dot{M}_* Z_{\rm ISM}$. We also consider an alternative formulation in which a fraction of SN-produced metals are directly ejected from the galaxy and only a fraction $f_{\rm ret}$ are retained within the star-forming ISM. In this case, all yields are multiplied by the factor $f_{\rm ret}$, which we assume to be the same for CCSNe and SNe Ia because without [α/Fe] measurements we have little leverage to separate the two retention factors. The outflows described by η are still assumed to be at the ISM metallicity, but the total metal loss rate is larger because of the direct ejection, which implicitly occurs at a rate $y(1 - f_{\rm ret})\dot{M}_*$ for each channel. In our fiducial model, we fix $f_{\rm ret} = 1$, reproducing the scenario in which all SN-produced metals are deposited initially into the star-forming ISM.

3.1.4 Initial and final conditions

Initial conditions of the model are largely set by the aforementioned model parameters. An exponential SFH as assumed in our fiducial model requires that Eri II begin with a non-zero gas mass at $t = 0$ Gyr such that

$$M_g(t = 0) = \tau_{\rm SFE}\dot{M}_*(t = 0). \quad (5)$$

This initial gas mass is assumed to be primordial in composition (e.g. $Z = 0$). The stellar mass of Eri II at $t = 0$ Gyr is assumed to be zero.

The evolution of the model effectively ends when the SFR is abruptly truncated at $t = t_{\rm trunc}$. Within the framework of this model, such a truncation could be achieved by removing all gas from the ISM and shutting off gas accretion (e.g. setting $M_g = \dot{M}_{\rm inf} = 0$), by heating gas in the ISM such that it cannot form stars (e.g. setting $\tau_{\rm SFE} = \infty$), or some combination of these effects. Both ram pressure stripping and reionization provide plausible physical explanations for the truncation of star formation, though the latter seems more likely given Eri II's relative isolation. We do not attempt to include a more detailed prescription for star formation truncation as our data set is of insufficient size and quality to yield meaningful insight.

Finally, all model parameters listed in Table 1 are assumed to be constant throughout Eri II's evolution, though we do not expect this to be strictly true in reality. For example, SN yields might vary with stellar metallicity, and the mass-loading factor could decrease over cosmic time as the mass of Eri II's dark matter halo grows. We leave more detailed analysis using time- and metallicity-dependent parameters for future study, noting that the parameters used in this work can be thought of as time-averaged quantities characteristic of Eri II's evolution.

3.1.5 Constructing the MDF

The number of stars born as a function of metallicity predicted by the model can be defined using the chain rule in terms of the SFR

[2] As discussed in WAF17, we approximate the power-law distribution using a sum of two exponentials to allow for an analytic solution.

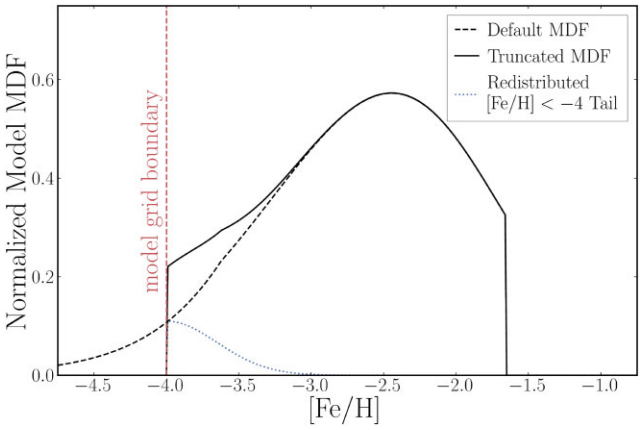

Figure 2. Example model MDF (see Section 3.1) before and after truncation below [Fe/H] < -4 (dashed and solid black lines, respectively). The dotted blue line illustrates the redistribution of the truncated probability following a half-normal distribution with $\sigma = 0.35$ dex. This model was generated with the following parameters: $\tau_{\rm SFE} = 100$ Gyr, $\tau_{\rm SFH} = 0.5$ Gyr, $t_{\rm trunc} = 1.0$ Gyr, and $\eta = 50$.

and the rate of change in [Fe/H] with time:

$$\frac{{\rm d}N}{{\rm d[Fe/H]}} = \frac{{\rm d}N/{\rm d}t}{{\rm d[Fe/H]}/{\rm d}t} \propto \frac{\dot{M}_*}{{\rm d[Fe/H]}/{\rm d}t}. \tag{6}$$

We caution that equation (6) only holds for a monotonically increasing [Fe/H], which is universally true for the WAF17 model. Time-steps of ${\rm d}t = 10^{-5}$ Gyr and metallicity sampling of d[Fe/H] $=$ 0.01 dex sufficiently minimize numerical artefacts. To convert between mass fractions of Fe and Mg predicted by the model and solar-scaled abundances [Fe/H] and [Mg/H], we adopt the photospheric abundance scale from Asplund et al. (2009), corresponding to solar mass fractions of 0.0013 and 0.0056, respectively. This choice of solar abundance scale purposefully matches the solar abundance scale used by the MIST isochrones that underpin the F22 CaHK measurements.

3.2 Likelihood and priors

We employ Bayesian hierarchical modelling to fit our chemical evolution model to the MDF of Eri II. As in previous analyses of dwarf galaxy MDFs (e.g. Kirby et al. 2011), we normalize the metallicity distribution, dN/d[Fe/H], predicted by our chemical evolution model (equation 6) such that $\int_{-\infty}^{\infty} {\rm d}N/{\rm d[Fe/H]}\ {\rm d[Fe/H]} = 1$ and adopt it as a probability distribution function (PDF) for the observed stellar abundances.

To account for the lower limit on observed [Fe/H] imposed by the MIST isochrone grid, we truncate this PDF below [Fe/H] < -4.0 and redistribute the truncated mass at the boundary following a half-normal distribution with width $\sigma = 0.35$ dex in accordance with the median measurement uncertainty from F22. We present an example of a (non-)truncated PDF predicted by the model in Fig. 2.

Unlike in previous studies, we do not directly incorporate the observed [Fe/H] abundances into our likelihood function. Instead, we adopt the posterior distributions from F22 (described in Section 2) as priors on the 'latent' [Fe/H] of each star, which we denote with a prime:

$$P_{\rm prior}([{\rm Fe/H}]_i') = P_{\rm Fu22}([{\rm Fe/H}] = [{\rm Fe/H}]_i' | {\rm CaHK}_i). \tag{7}$$

These latent abundances, $[{\rm Fe/H}]_i'$, are fit simultaneously along with the free model parameters ($\tau_{\rm SFE}$, $\tau_{\rm SFH}$, $t_{\rm trunc}$, η, and where relevant $f_{\rm ret}$). The total log-likelihood is then

$$\ln \mathcal{L} = \sum_{i=1}^{N_*} \ln \left.\frac{{\rm dN}}{{\rm d[Fe/H]}}\right|_{[{\rm Fe/H}]_i'}, \tag{8}$$

where the sum is over all N_* observed stars and the PDF, dN/d[Fe/H], is evaluated at the latent abundance $[{\rm Fe/H}]_i'$ of each star. Equation (8) ensures that we do not infer an $[{\rm Fe/H}]_i'$ for any star beyond the maximum [Fe/H] predicted by the model, while equation (7) penalizes the model for requiring $[{\rm Fe/H}]_i'$ values in tension with the ${\rm CaHK}_i$ measurements.

We adopt a truncated Gaussian prior on the SFH time-scale, $\tau_{\rm SFH}$, centred at 0.7 Gyr with width 0.3 Gyr and bounded to be positive definite:[3]

$$\tau_{\rm SFH} \sim \mathcal{TN}(0.7, 0.3, 0.0, \infty).$$

This choice of prior is informed by Gallart et al. (2021) who derived an SFH from deep *HST*/ACS photometry of Eri II that is peaked at the oldest possible age with half-width at half-maximum (HWHM) of $\sim$0.5 Gyr corresponding to a $\sim$0.7 Gyr e-folding time-scale for an exponentially declining SFH. While a negatively skewed prior may be appropriate – Gallart et al. (2021) suggest that the true duration of Eri II's burst of star formation is likely unresolved by their study and could be as short as 100 Myr – we adopt a Gaussian prior for simplicity.

Similarly, we adopt a positive definite truncated Gaussian prior on the SFH truncation time, $t_{\rm trunc}$, centred at 1 Gyr with width 0.5 Gyr.

$$t_{\rm trunc} \sim \mathcal{TN}(1.0, 0.5, 0.0, \infty).$$

This too is motivated by the lack of evidence found by Gallart et al. (2021) for star formation in Eri II within the last $\sim$13 Gyr.

We utilize broad uniform priors for the remaining model parameters as follows:[4]

$$\log_{10} \tau_{\rm SFE} \sim \mathcal{U}(0.0, 4.0),$$
$$\eta \sim \mathcal{U}(0.0, 10^3).$$

Note that we have reparametrized to fit for $\tau_{\rm SFE}$ in log-space given the large dynamic range we wish to explore.

Together, the sum of the 64 log-priors (4 for the model parameters and 1 for each of the stars' [Fe/H]′) and the log-likelihood presented in equation (8) yield the log-posterior distribution that we wish to sample.

3.3 Alternative models

In addition to the fiducial model described above, we consider several alternative models to build physical intuition and test specific scenarios. We briefly describe the motivation and adjustments for each below. Any parameters not explicitly referenced are identical to those in the fiducial model (Table 1).

Linear-exponential SFR model. In the fiducial model, we assume an exponentially declining SFR, which requires a non-zero gas mass at the onset of star formation. With this model, we test an alternative

[3]Throughout this work, we adopt the following notation for the truncated normal distribution: $X \sim \mathcal{TN}(\mu_X, \sigma_X, X_{\rm min}, X_{\rm max})$, where μ_X, σ_X, $X_{\rm min}$, $X_{\rm max}$ are respectively the mean, standard deviation, lower bound, and upper bound of the distribution.

[4]Throughout this work, we adopt the following notation for the uniform distribution: $X \sim \mathcal{U}(X_{\rm min}, X_{\rm max})$, where $X_{\rm min}$ and $X_{\rm max}$ are lower and upper bounds of the distribution, respectively.

'linear-exponential' functional form for the SFR functional form, given by

$$\dot{M}_* \propto \begin{cases} t \exp(-t/\tau_{\rm SFH}), & \text{if } t \leq t_{\rm trunc} \\ 0, & \text{if } t > t_{\rm trunc} \end{cases}. \quad (9)$$

In this model, the need for an initial gas reservoir is avoided as the galaxy begins with no star formation at $t = 0$ Gyr. Rather, the SFR increases rapidly from zero to its peak at $t = \tau_{\rm SFH}$ before declining more gradually. As in the fiducial case, we adopt a prior for $\tau_{\rm SFH}$ motivated by the ∼0.5 Gyr SFH HWHM measured by Gallart et al. (2021). For the above linear-exponential SFH, this corresponds to $\tau_{\rm SFH} \sim 0.2$ Gyr, and so we use the following truncated Gaussian prior:

$$\tau_{\rm SFH} \sim \mathcal{TN}(0.2, 0.1, 0.0, \infty).$$

Constant SFR model. With this model, we test whether a constant SFR could reproduce Eri II's MDF. No $\tau_{\rm SFH}$ is fit for this model as a constant SFR is equivalent to letting $\tau_{\rm SFH} \to \infty$.

Metal-loading model. In this model, we enable SN-produced metals to be directly ejected from the galaxy by allowing a non-zero retention factor. Specifically, we adopt a uniform prior on $f_{\rm ret}$:

$$f_{\rm ret} \sim \mathcal{U}(0.0, 1.0).$$

Due to the large degeneracy between $f_{\rm ret}$ and η, we find it desirable to impose a tight prior on η, which we force to be roughly four times smaller than preferred in the fiducial case (see Section 4):

$$\eta \sim \mathcal{N}(50, 10).$$

While we do achieve converged Monte Carlo chains with $f_{\rm ret}$ and η both free (see Section 3.4), the degeneracy between the parameters makes the results hard to interpret.

High SFE model. With this model, we investigate whether the MDF of Eri II can be modelled assuming a short SFE time-scale of $\log_{10}\tau_{\rm SFE} \sim 0.4$, which is roughly an order of magnitude smaller than preferred by the fiducial model (see Section 4). Such a high SFE might be expected if a large fraction (∼75 per cent) of Eri II's gas was in the molecular phase. We force this enhanced SFE by implementing a tight prior on $\log_{10}\tau_{\rm SFE}$ of

$$\log_{10}\tau_{\rm SFE} \sim \mathcal{N}(0.4, 0.1).$$

Longer SN Ia delay model. In the fiducial model, we implement a minimum time delay for SN Ia of $t_{\rm D} = 0.05$ Gyr corresponding to the lifetimes of the most massive SN Ia progenitors. However, previous chemical evolution studies (e.g. Schönrich & Binney 2009; Andrews et al. 2017) have adopted a slightly longer time delay of 0.15 Gyr before the first SN Ia. In this model, we set $t_{\rm D} = 0.15$ Gyr to test the impact of assuming a more delayed onset of SN Ia.

No SN Ia model. To evaluate the importance of SN Ia enrichment on the shape of Eri II's MDF, we consider a scenario in which SN Ia do not contribute at all to the enrichment of the galaxy. In this model, we set $y^{\rm Ia}_{\rm Fe} = 0$ but the same could be accomplished by setting $f^{\rm Ia}_{\rm ret} = 0$.

Enhanced SN Ia model. In this model, we assume the specific SN Ia rate scales with metallicity proportional to $Z^{-0.5}$ as found in the recent analysis of Johnson et al. (2023a). For Eri II, this scaling would imply an enhancement of the SN Ia rates by roughly an order of magnitude, which we implement by simply increasing the fiducial SN Ia Fe yield $y^{\rm Ia}_{\rm Fe}$ by a factor of 10 to $y^{\rm Ia}_{\rm Fe} = 0.012$.

3.4 Sampling

To sample our posterior distributions, we employ the *Preconditioned Monte Carlo* (PMC) method for Bayesian inference implemented in the publicly available PYTHON package POCOMC[5] (Karamanis et al. 2022a, b). PMC uses a combination of a normalizing flow with a sequential Monte Carlo sampling scheme to decorrelate and efficiently sample high-dimensional distributions with non-trivial geometry.

We initialize 5000 walkers from the prior distributions described in Section 3.2, imposing an arbitrary log-posterior threshold to ensure walkers are not too distant from the bulk of the posterior mass. We adopt default hyperparameters for POCOMC, run until the sampler has converged (i.e. when the 'inverse temperature' $\beta = 1$), and then draw an additional 5000 samples for a total of 10 000 samples from the posterior distribution.

4 RESULTS

4.1 Fiducial fit to Eri II MDF

We begin by briefly summarizing the recovered posterior distribution for the model parameters $\log_{10}\tau_{\rm SFE}$, $\tau_{\rm SFH}$, $t_{\rm trunc}$, and η, which we display in Fig. 3. For each parameter, we report the median of each marginalized posterior distribution (blue lines) and the 16th and 84th percentiles (dashed black lines) in Table 2; for brevity, we refer to the posterior medians as 'best-fitting' values hereafter, with the percentile ranges treated as $\pm1\sigma$ uncertainties. These are discussed individually in Section 4.1.1. In short, we find that the MDF of Eri II is sufficient to place constraints on $\log_{10}\tau_{\rm SFE}$ ($1.44\pm^{0.28}_{0.27}$), $\tau_{\rm SFH}$ ($0.39\pm^{0.18}_{0.13}$ Gyr), and η ($194.53\pm^{33.37}_{42.67}$) but not $t_{\rm trunc}$ ($1.37\pm^{0.37}_{0.37}$ Gyr), which remains prior-dominated. We explore the aspects of the MDF's shape that contribute to these constraints (or lack thereof) in Appendix A.

Importantly, we find that our fiducial model produces realistic predictions for the Eri II MDF, which we illustrate in Fig. 4 using both continuous (top panel) and binned (middle panel) representations. The blue dashed lines in these panels represent the latent MDFs for the best-fitting model parameters, which is the sum of the latent posterior distributions of the individual stars (in the top panel) integrated over the bins (in the middle panel). To visualize the uncertainties on the latent MDF, we make a bootstrap selection from our set of 60 stars (allowing replacement) and draw from the star's latent [Fe/H] posterior distribution, capturing both the uncertainties from finite sample size and the measurement uncertainties for each star. The resulting 95 per cent confidence interval is depicted by the blue-shaded region. The best-fitting model MDF (thick red line) is in good agreement with the latent MDF, predicting a negatively skewed distribution with a small low-metallicity tail and little to no truncation below the model grid boundary. We additionally perform a posterior predictive check of our model by generating model MDFs for 1000 random draws from the parameter posteriors (thin red lines), which illustrates the range of MDFs consistent with the uncertainties on our best-fitting model parameters. We include the observed CaHK [Fe/H] MDF from F22 (solid gray line) for reference, but reiterate that reproducing the latent MDF, not the input CaHK MDF, maximizes the likelihood.

In the bottom panel of Fig. 4, we present the posterior distribution for each of the 60 stars' underlying [Fe/H]. Compared to the input

[5] https://github.com/minaskar/pocomc

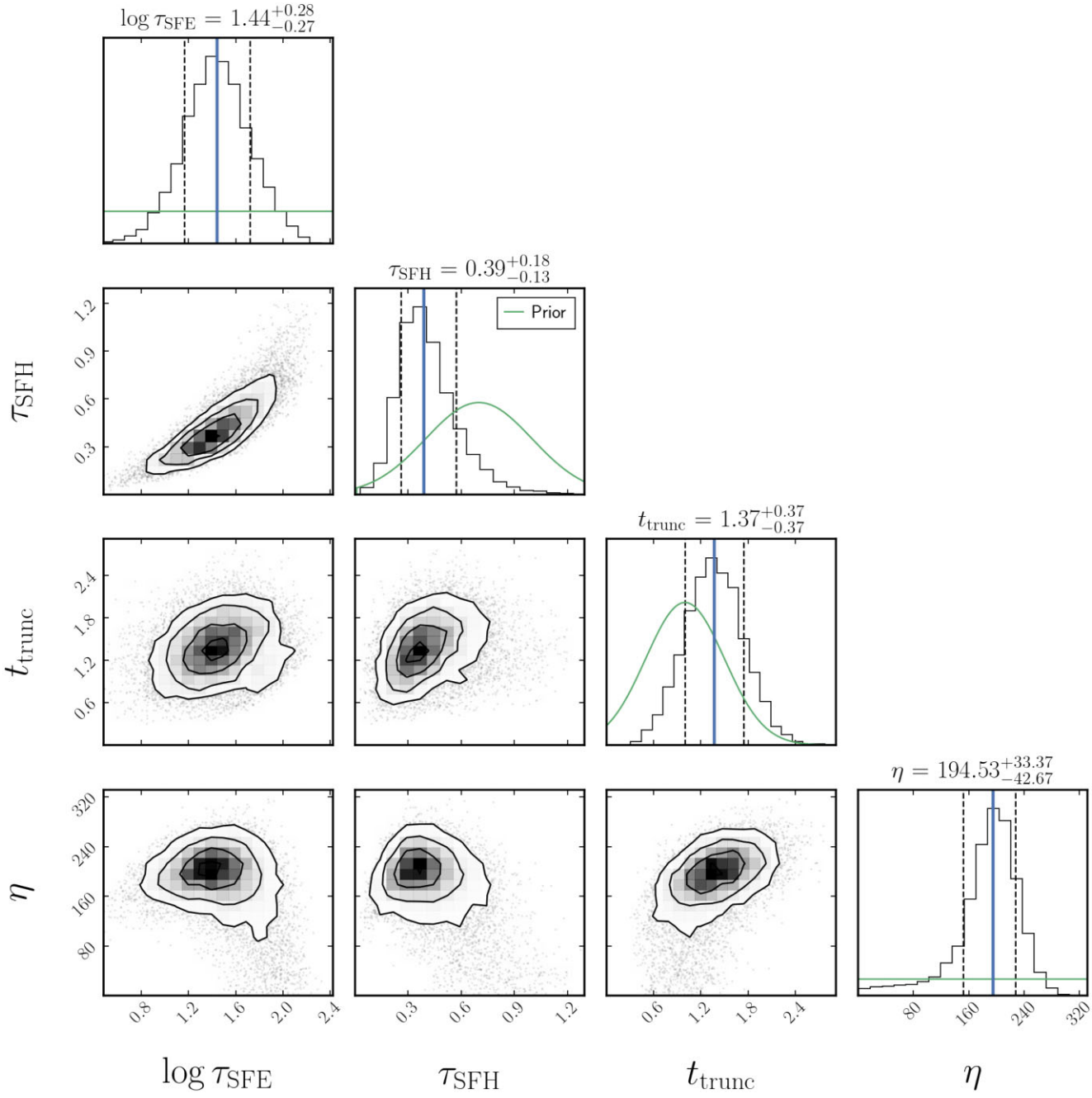

Figure 3. Posterior distribution corner plot of the model parameters $\log_{10}\tau_{\rm SFE}$, $\tau_{\rm SFH}$, $t_{\rm trunc}$, and η. Median values and 1σ uncertainties from the 16th and 84th percentiles are reported for each label and denoted by vertical solid blue and dashed black lines, respectively. The adopted prior distributions are included for reference as solid green lines. The Eri II MDF provides informative constraints on $\log_{10}\tau_{\rm SFE}$, $\tau_{\rm SFH}$, and η, while $t_{\rm trunc}$ remains prior-dominated.

CaHK posteriors (Fig. 1; bottom panel), these updated posteriors exhibit less pronounced low-metallicity tails as well as less frequent and less severe truncation at the model boundary of [Fe/H] = −4. The mean metallicity, $\langle$[Fe/H]$\rangle = -2.52\pm^{0.04}_{0.04}$, and metallicity dispersion, $\sigma_{\rm [Fe/H]} = 0.45\pm^{0.04}_{0.04}$, are still in good agreement with the values found by F22.

4.1.1 *Inferred parameters of Eri II*

Star formation efficiency. We infer the log-SFE time-scale of Eri II to be $\log_{10}\tau_{\rm SFE} = 1.44\pm^{0.28}_{0.27}$ ($\tau_{\rm SFE} = 27.56\pm^{25.14}_{12.92}$ Gyr) or in terms of the SFE ($\tau^{-1}_{\rm SFE}$): SFE $= 0.036\pm^{0.032}_{0.017}$ Gyr^{-1}. This time-scale is quite large compared to the SFE time-scale of molecular gas ($\tau_{\rm SFE} = 2$ Gyr; Leroy et al. 2008) but in line with the current paradigm that low-mass galaxies are the least efficient at converting their gas into stars (e.g. Behroozi, Wechsler & Conroy 2013, and references therein).

In Fig. 5, we compare the inferred SFE of Eri II with the best-fitting SFE reported by previous chemical evolution studies of 13 LG dwarf galaxies spanning a wide range in stellar masses (Lanfranchi & Matteucci 2004, 2007, 2010; Lanfranchi, Matteucci & Cescutti 2006; Vincenzo et al. 2014; Romano et al. 2015; Lacchin et al. 2020; Alexander et al. 2023). Here, we adopt a stellar mass for Eri II of

Table 2. Inferred Eri II parameters. Median values and 1σ uncertainties inferred for the model parameters from the fiducial and alternative model fits. Values without uncertainties were held fixed. The estimated BF relative to the fiducial model is presented in the rightmost column.

Model	$\log_{10}\tau_{\rm SFE}$	$\tau_{\rm SFH}$ [Gyr]	$t_{\rm trunc}$ [Gyr]	η	$f_{\rm ret}$	t_D [Gyr]	$y^{\rm Ia}_{\rm Fe}$	BF
Fiducial	$1.44\pm^{0.28}_{0.27}$	$0.39\pm^{0.18}_{0.13}$	$1.37\pm^{0.37}_{0.37}$	$194\pm^{43}_{33}$	1	0.05	0.0012	1.000
Linear-exponential SFR	$1.41\pm^{0.22}_{0.23}$	$0.21\pm^{0.06}_{0.06}$	$1.26\pm^{0.36}_{0.32}$	$186\pm^{35}_{40}$	1	0.05	0.0012	3.099
Constant SFR	$1.85\pm^{0.18}_{0.23}$	∞	$1.03\pm^{0.37}_{0.34}$	$17\pm^{21}_{12}$	1	0.05	0.0012	0.232
Metal loading	$1.00\pm^{0.48}_{0.34}$	$0.47\pm^{0.19}_{0.16}$	$1.26\pm^{0.39}_{0.38}$	$52\pm^{8}_{8}$	$0.32\pm^{0.22}_{0.07}$	0.05	0.0012	0.711
High SFE	$0.47\pm^{0.08}_{0.08}$	$0.08\pm^{0.04}_{0.08}$	$1.06\pm^{0.39}_{0.37}$	$145\pm^{37}_{30}$	1	0.05	0.0012	0.002
Longer SN Ia delay	$1.44\pm^{0.23}_{0.21}$	$0.49\pm^{0.16}_{0.14}$	$1.33\pm^{0.35}_{0.34}$	$155\pm^{31}_{35}$	1	0.15	0.0012	1.018
No SN Ia	$1.57\pm^{0.23}_{0.18}$	$0.45\pm^{0.21}_{0.18}$	$1.26\pm^{0.36}_{0.33}$	$71\pm^{21}_{39}$	1	0.05	0.0000	2.239
Enhanced SN Ia	$1.44\pm^{0.48}_{0.31}$	$0.48\pm^{0.18}_{0.12}$	$1.06\pm^{0.32}_{0.27}$	$879\pm^{61}_{91}$	1	0.05	0.0120	0.024

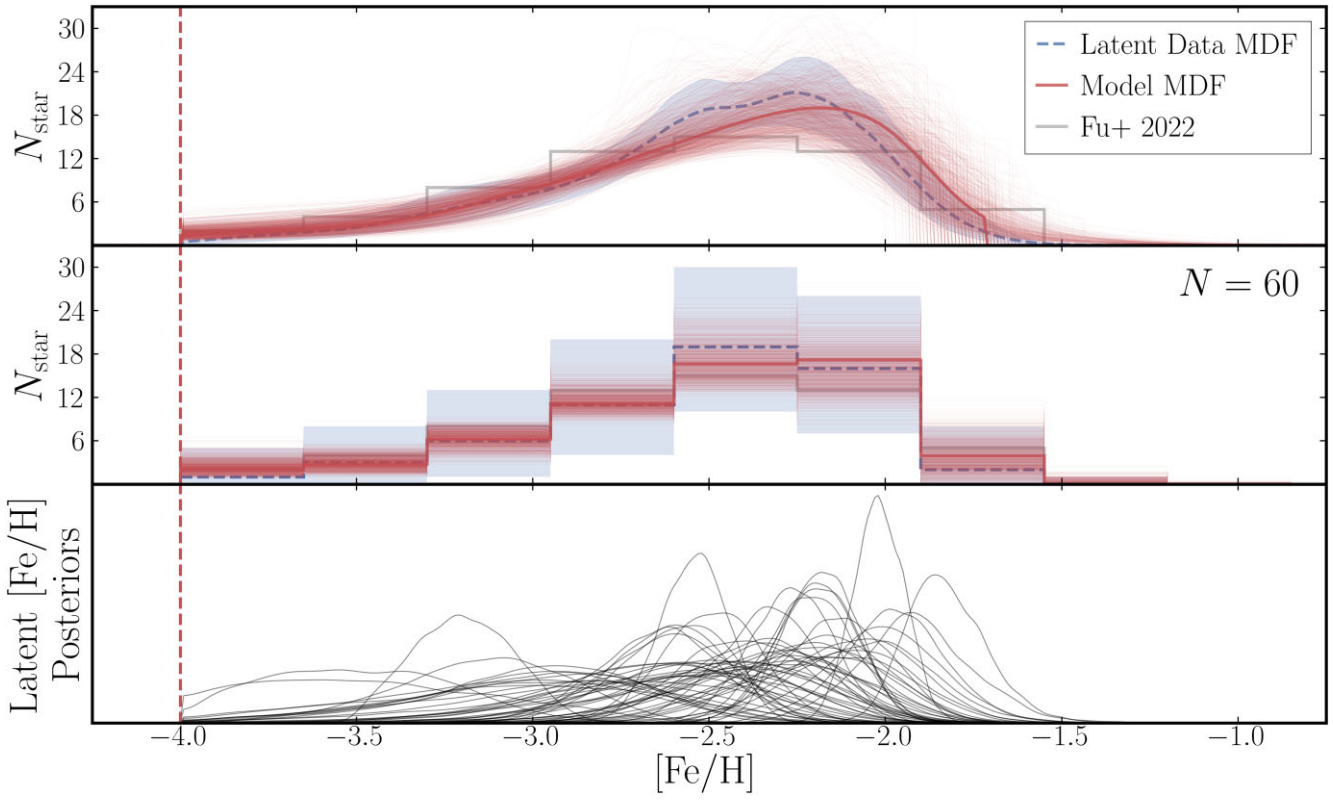

Figure 4. Top: best-fitting model MDF (solid red line; computed from the parameter values listed in Table 2) compared to the latent [Fe/H] MDF (dashed blue line). Uncertainties on the latent MDF (blue-shaded regions) are estimated via bootstrapping (with replacement) from our sample of stars and drawing from each star's latent [Fe/H] posterior distribution. Model MDFs generated from 1000 random draws of the posterior distribution are displayed in thin red lines. We include the observed CaHK [Fe/H] MDF from F22 (solid grey line; same as in Fig. 1) for reference but note that the model is not directly fit to this MDF. Middle: same as the top panel but binned for comparison to the F22 CaHK MDF. Bottom: updated posteriors distributions of [Fe/H] for each star in the sample. Compared to the CaHK posteriors presented in the bottom panel of Fig. 1, long low-metallicity tails and the degree of truncation at [Fe/H] $= -4$ are substantially reduced because the model predicts that only a small fraction of stars have such low metallicities. Our fit indicates that it is unlikely that any of the stars in our sample are truly UMP stars with [Fe/H] $\lesssim -4$.

2×10^5 $M_\odot$ from Gallart et al. (2021). Despite the range in chemical evolution models and assumptions adopted in these studies, a clear trend between a galaxy's SFE and its stellar mass is visible. As expected, galaxies more massive than Eri II are found to be more efficient at converting gas to stars (SFE $\sim$ 0.5–1.0 $\rm Gyr^{-1}$), while galaxies less massive than Eri II are found to be less efficient (SFE $\sim$ 0.003–0.03 $\rm Gyr^{-1}$). Given this apparent relationship, the SFE we infer for Eri II is in good agreement with expectations given its stellar mass.

A low SFE like that found for Eri II may be indicative that the majority of Eri II's gas is in the atomic phase. Following the reasoning of Johnson & Weinberg (2020) that $\tau_{\rm SFE} = (2\ {\rm Gyr})(1 + M_{\rm HI}/M_{\rm H_2})$, we infer that the molecular gas fraction in Eri II was only $7.26\pm^{6.41}_{3.46}$ per cent. This, of course, is only a rough approximation given the assumptions made in our model. It is possible that the molecular gas fraction of Eri II changed over its star-forming lifetime, resulting in a time-varying SFE. WAF17 find that smooth evolution of $\tau_{\rm SFE}$ has little impact on chemical evolution tracks if the SFH remains

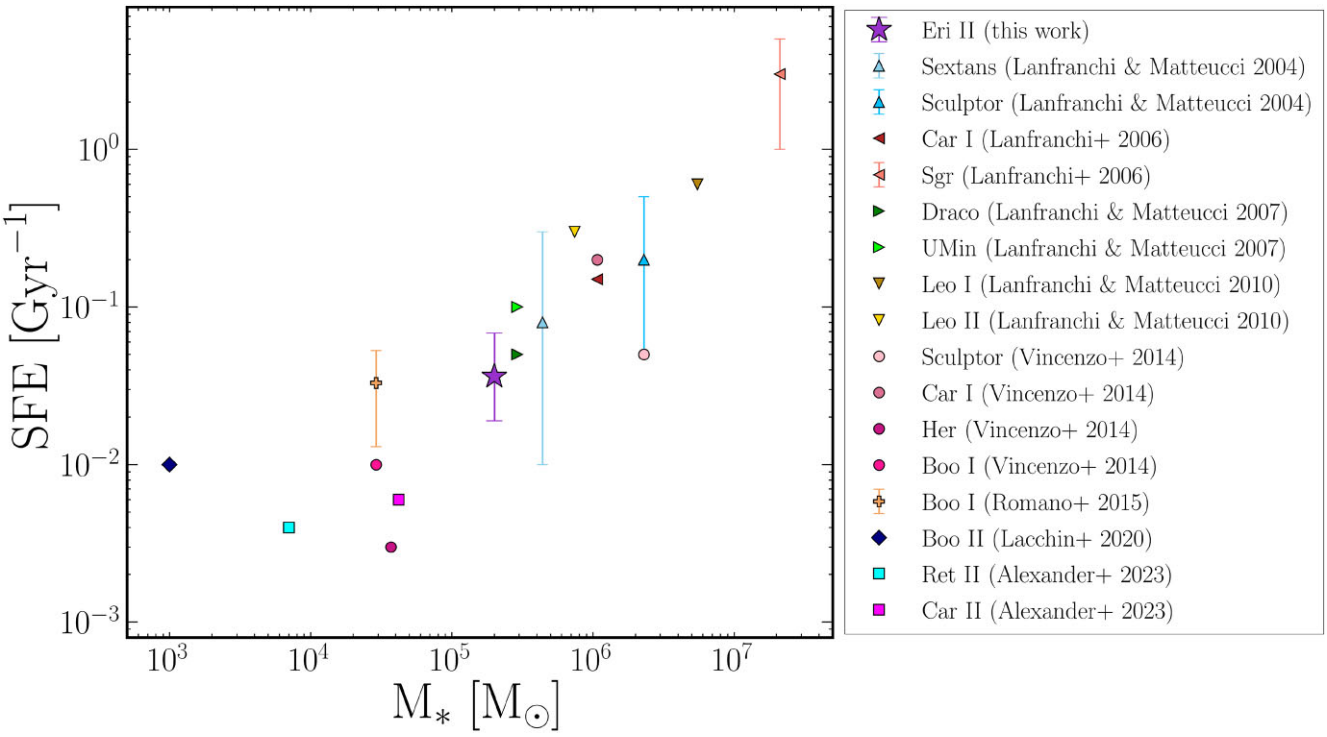

Figure 5. The inferred SFE of Eri II (purple star) compared to the SFEs reported by previous chemical evolution studies of LG dwarf galaxies. Though these studies employed a range of chemical evolution models, a clear relationship between galaxy stellar mass and SFE is apparent. The SFE inferred for Eri II is in good agreement with this relationship given its stellar mass.

fixed, but we have not yet investigated the low-metallicity regime relevant here. While numerical solutions with time-dependent SFE are feasible, it is not clear what behaviour would be appropriate to assume for Eri II, and so we stick with the simplest assumption of constant SFE.

Star formation history. We recover the SFH time-scale of Eri II to be $\tau_{\rm SFH} = 0.39\pm^{0.18}_{0.13}$ Gyr. This is slightly shorter than the SFH reported by Gallart et al. (2021), which informed our choice of prior ($\tau_{\rm SFH,\ prior} = 0.7 \pm 0.3$ Gyr). The SFH time-scale we infer corresponds to a star formation HWHM of $270\pm^{130}_{90}$ Myr – about half the duration found by Gallart et al. (2021). This supports the hypothesis of Gallart et al. (2021) that the true duration of Eri II's main star formation episode is shorter than they could resolve with their color-magnitude diagram (CMD) fitting techniques. Assuming star formation commenced immediately, the inferred $\tau_{\rm SFH}$ implies that Eri II had formed ∼65 per cent of its stellar mass by $z \sim 11.5$ per cent and ∼95 per cent of its stellar mass by $z \sim 5.7$, which would independently confirm that Eri II is a relic of pre-reionization era galaxy formation.

While we can place tight constraints on the SFH time-scale, the inference of $t_{\rm trunc}$ ($t_{\rm trunc} = 1.37\pm^{0.37}_{0.37}$ Gyr; $z_{\rm trunc} = 4.40\pm^{1.25}_{0.81}$) remains dominated by the imposed prior. Tests allowing $t_{\rm trunc}$ to be unconstrained find no evidence in Eri II's MDF that the SFR truncated abruptly within the first 5 Gyr. That said, we know from Eri II's CMD that there has been effectively no star formation for the last ∼13 Gyr. Our inability to provide independent constraints on $t_{\rm trunc}$ is not indicative of tension between the MDF and CMD but rather a result of how subtle the impact of truncation is given Eri II's short star formation time-scale. In our best-fitting model, truncation occurs after $\sim 3.5\tau_{\rm SFH}$, when the SFR is already quite low – Eri II's stellar mass would only increase by ∼3 per cent in the absence of truncation. In other words, the inferred exponential suppression of Eri II's SFH is already strong enough that a final, superexponential truncation is difficult to detect. Constraining a sharp truncation in Eri II's SFH from its MDF would require a larger sample of stars with abundance measurements precise enough to map the high-metallicity tail of the MDF.

4.1.1.3 Mass-loading factor We recover a broad but clearly peaked posterior for the galaxy's mass-loading factor, $\eta = 195\pm^{33}_{43}$. This means that for every 1 $M_\odot$ of star formation, nearly 200 $M_\odot$ of ISM gas is ejected from the galaxy by SNe feedback. While extreme in comparison to the mass-loading factors of MW-like galaxies ($\eta \sim 1$), mass-loading factors of this magnitude are frequently invoked for low-mass galaxies in order to match simulations to empirical scaling relations (e.g. Benson et al. 2003; Somerville & Davé 2015; Mitchell et al. 2020). State-of-the-art hydrodynamic simulations have also found $\eta \sim 100$ for the lowest-mass dwarf galaxies (e.g. Muratov et al. 2015; Emerick, Bryan & Mac Low 2019; Pandya et al. 2021).

In Fig. 6, we compare our inferred mass-loading factor for Eri II (purple star) to the mass-loading factors inferred from chemical evolution studies of the disrupted dwarf galaxies *Gaia*-Sausage Enceladus (GSE) and Wukong/LMS-1 by Johnson et al. (2023b) using the `VICE` one-zone chemical evolution model (red and blue circles, respectively) and of the UFDs Carina II and Reticulum II by Alexander et al. (2023) using the `i-getool` inhomogenous chemical evolution model (magenta and cyan squares, respectively). In addition, we include measurements of the mass-loading factor of galaxies from Chisholm et al. (2017) and McQuinn et al. (2019, black diamonds and triangles respectively). Lastly, we include the dwarf starburst galaxy Pox 186, which was observed by Eggen et al. (2021) to currently have a suppressed mass-loading factor (open black pentagon) due to the efficient removal of gas by earlier SN-driven

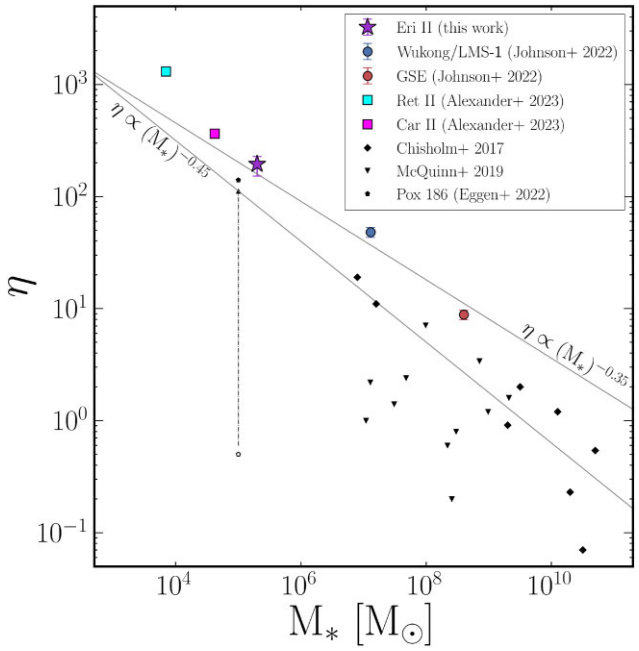

Figure 6. The inferred mass-loading factor of Eri II (purple star) compared to the mass-loading factors inferred by the chemical evolution studies of Johnson, Kochanek & Stanek (2023b) for Wukong/LMS-1 and GSE (blue and red circles, respectively) and Alexander et al. (2023) for Car II and Ret II (magenta and cyan squares, respectively) as a function of stellar mass. Mass-loading factors for galaxies observed by Chisholm et al. (2017) and McQuinn, van Zee & Skillman (2019) are included as black diamonds and triangles, respectively. The current observed mass-loading factor of Pox 186 and its previous estimated mass-loading factor from Eggen et al. (2021) are represented by the open and filled black pentagons, respectively. The scaling found by Muratov et al. (2015) in FIRE-1 simulations indicative of momentum-driven winds ($\eta \propto M_*^{-0.35}$) and the scaling found by Pandya et al. (2021) in FIRE-2 simulations indicative of energy-driven winds ($\eta \propto M_*^{-0.45}$) are included for reference as solid black lines.

outflows. By estimating the total amount of gas lost to outflows, Eggen et al. (2021) concluded that the mass-loading factor of Pox 186 was substantially larger during its previous outflow episode (filled black pentagon).

Direct comparison between mass-loading factors measured through direct observational indicators (e.g. Chisholm et al. 2017; McQuinn et al. 2019) and chemical evolution models (Alexander et al. 2023; Johnson et al. 2023b, and this work) is challenging for a number of reasons. For one, the manner in which outflows are parametrized in models frequently do not map directly to the observable quantities being measured. Additionally, the strength of outflows experienced presently at $z = 0$ by a galaxy of a given mass may not be representative of the outflows experienced at high redshift by galaxies of a similar mass. Nevertheless, our result for Eri II is in good qualitative agreement with the observed trend that less massive galaxies have stronger outflows.

Two scaling relationships have historically been invoked for relating the mass-loading factor of a galaxy to its stellar velocity dispersion, σ (as a proxy for its mass). In the physical scenario of momentum-driven winds governed by radiation pressure, the mass-loading factor scales as $\eta \propto V_c^{-1}$ (Murray, Quataert & Thompson 2005). This scaling has been argued for by Finlator & Davé (2008) and Peeples & Shankar (2011) based on the observed mass–metallicity relationship. Based on results from the Feedback in Realistic Environments (FIRE-1) cosmological zoom-in simulation (Hopkins et al. 2014), Muratov et al. (2015) found a scaling relationship between the mass-loading factor and galactic stellar mass of $\eta = 3.6(M_*/10^{10}\ \mathrm{M}_\odot)^{-0.35}$, which is in good agreement with the expectations given a momentum-driven wind scaling. Alternatively, in the physical scenario of energy-driven winds from SNe, the mass-loading factor scales as $\eta \propto V_c^{-2}$ (Chevalier & Clegg 1985). This scaling has been argued to be more important in low-mass galaxies with $\sigma < 75$ km s^{-1} (e.g. Murray et al. 2005, 2010; Hopkins, Quataert & Murray 2012; Davé et al. 2013). Furthermore, Pandya et al. (2021) found a steeper scaling relationship in the updated FIRE-2 simulations (Hopkins et al. 2018) of $\eta = 0.6(M_*/10^{10}\ \mathrm{M}_\odot)^{-0.45}$, which is more characteristic of the energy-driven wind scaling.

For reference, we have included both the momentum-driven scaling ($\eta \propto M_*^{-0.35}$) of Muratov et al. (2015) and the energy-driven scaling ($\eta \propto M_*^{-0.45}$) of Pandya et al. (2021) in Fig. 6. The normalization of the chemistry-based mass-loading factors, including Eri II, is more in-line with the findings of Muratov et al. (2015). However, their scaling with stellar mass is marginally closer to that of Pandya et al. (2021), just offset by a small factor to larger values. A larger sample of galaxies, especially at the lowest masses, is required before these measurements can discriminate between these two physical outflow scenarios.

While smaller mass-loading factors ($\eta \lesssim 50$) are not prohibited by the model, they are 2σ disfavoured and would require longer SFE and SFH time-scales. Allowing for direct ejection of SN products (e.g. letting $f_{\rm ret} < 1$) has the potential to temper large mass-loading factors, but preliminary tests suggest that (1) mass-loading values of $\eta \sim 100$ are still preferred and (2) lower mass-loading factors require both low retention fractions ($f_{\rm ret} \sim 0.3$) and higher SFEs ($\tau_{\rm SFE} \sim 1.0$) – see Section 4.2.3. Adopting lower stellar iron yields like those proposed in Weinberg et al. (2023) may also resolve some of the tension between the directly observed and chemically inferred mass-loading factors.

As with the $\tau_{\rm SFE}$, η could in principle vary with time as Eri II's dark matter halo grew and its potential well deepened, though large changes in η over the duration of Eri II's star-forming lifetime are disfavoured by its small $\tau_{\rm SFH}$. We leave investigation of a time-dependent η for future study.

4.2 Alternative model fits

Here we present the results of fitting the Eri II MDF with the alternative models described in Section 3.3. Median and 16th and 84th percentiles of the marginalized posteriors are presented alongside the fiducial best-fitting values in Table 2. In Fig. 7, we compare the MDF predicted for these median posterior values of each alternative model (coloured lines) to that of the fiducial model (black line) and its latent [Fe/H] distribution (gray dashed line and shaded region). We refer to these predicted MDFs as the 'best fit' for each model, though strictly speaking the model with the highest posterior probability does not have exactly the median posterior values of each parameter.

It is not entirely fair to judge the quality of the alternative model fits to the fiducial latent MDF, as each model may predict a different underlying distribution. In practice, however, we find that latent MDF of most models is quite similar to the fiducial case. The two exceptions to this are the latent distributions of the constant SFR and high SFE models, which are more negatively skewed and centrally peaked, respectively. While not statistically prohibited given the wide posteriors of the CaHK measurements, such underlying MDFs would be unusual in comparison to the MDFs observed in other dwarf galaxies using more precise spectroscopic abundances.

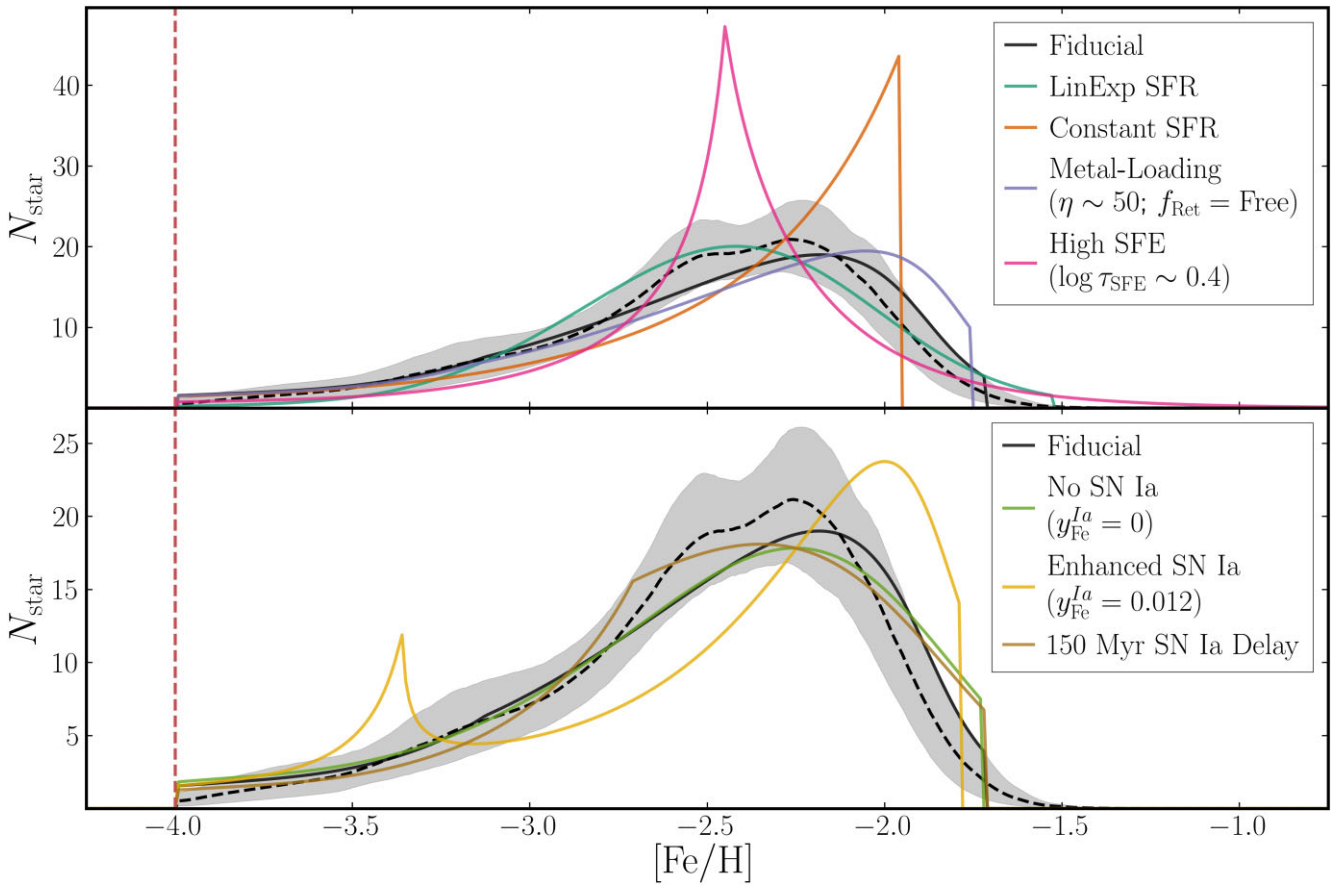

Figure 7. Best-fitting MDFs generated with the alternative models described in Section 3.3 (coloured lines) compared to the fiducial model's best-fitting MDF (solid black line) and latent [Fe/H] distribution (dashed black line and grey-shaded region).

One quantitative metric for judging the goodness of fit of each model relative to the fiducial model is the Bayes factor (BF). The BF is defined as the ratio of the Bayesian evidence of each model, which expresses the posterior probability of one model relative to the fiducial model under the a priori assumption that both models are equally probable. A BF < 1 indicates that the fiducial model is more probable while a BF > 1 indicates the alternative model is more probable. Using the Bayesian evidence estimated by POCOMC, we calculate the BF for each model; we present these in the rightmost column of Table 2.

In general, we find BFs < 1, indicating that the fiducial model is preferred. However, we caution that the BF is inherently sensitive to choices in priors, so BFs of $\mathcal{O}(1)$ should not be overinterpreted. Nevertheless, because the BFs of the high SFE and enhanced SN Ia are $\ll 1$, we can be fairly confident that those models are disfavoured. With a BF of $\sim$0.2, the constant SFR model is also disfavoured but to a more modest degree. One could argue that many of the alternative models require specific values for model parameters, making them a priori less likely. In this case, the BF we calculate would overestimate the probability of the alternative models relative to the fiducial model. Definitively ruling out alternative models with BF ~ 1 would require additional observational constraints, including a larger sample of stars, more precise [Fe/H] measurements, and/or measurements of [α/Fe]. To investigate the impact of increasing the sample size or measurement precision, we perform a suite of mock fits and compute the resulting changes in the alternative models' BFs. For a description of this procedure and detailed results, see Appendix B. For a discussion of [α/Fe], see Section 5.2.

We discuss each alternative model and their MDF predictions below.

4.2.1 *Linear-exponential SFR model*

Despite the distinctly different functional form of the linear-exponential SFR model, we find that it provides a fit to the data which is just as good (if not slightly better) than that of the fiducial model, while inferring very similar values for $\tau_{\rm SFE}$, $t_{\rm trunc}$, and η. Though the MDF predicted by this model is more symmetric, peaking at a slightly lower metallicity ([Fe/H] ~ -2.5) and extending to a higher metallicity ([Fe/H] ~ -1.5), the dispersion and mean metallicity of the MDF are in good agreement with the fiducial model's predictions. The BF slightly favours this fit over the fiducial, but only marginally so. We find that confidently discriminating between these two models would require a larger sample ($N_{\rm star} > 100$) of much more precise ($\lesssim$0.1 dex) stellar [Fe/H] measurements, placing such an endeavour out of reach for the foreseeable future.

Our primary conclusion from this model is that our constraints on $\tau_{\rm SFE}$ and η from the fiducial model are *not* sensitive to the assumed SFH at early times. In particular, our findings are insensitive to the fiducial model's assumption that Eri II's gas reservoir was already in place at the onset of star formation, instead of growing rapidly through gas accretion as it does in the linear-exponential SFR model (see Section 3.1.4).

4.2.2 *Constant SFR model*

The constant SFR model predicts an MDF that is rapidly increasing until it sharply truncates at the high-metallicity end. Such an MDF is atypical for dwarf galaxies in the LG, which universally exhibit MDFs that turn over at the high-metallicity end (e.g. Kirby et al. 2011). The outflow mass-loading required to achieve the observed metallicity range is an order of magnitude below that of the fiducial model because a constant SFR requires rapid continuing gas accretion that dilutes the metal production from stars. Relaxing the prior on $t_{\rm trunc}$ results in an earlier truncation ($\sim$0.6 Gyr) and a slightly smaller $\log_{10}\tau_{\rm SFE}$ ($\sim$1.7), but the shape of the predicted MDF and the inferred mass-loading factor remain largely the same. Although the predicted MDF shape is radically different from the F22 histogram and from the latent MDF of the fiducial model, the BF only mildly disfavours the constant SFR model. This is because some of the uncertainties in the CaHK [Fe/H] measurements are large enough ($\sim$0.3–0.5 dex) that the sharply truncated MDF of the constant SFR model is not in strong tension with the observations. We find that the constant SFR model could be easily ruled out if the measurement uncertainties could be reduced to $\lesssim$0.3 dex.

4.2.3 *Metal-loading model*

We find that forcing a lower mass-loading factor ($\eta \sim 50$) is able to produce realistic fits to the Eri II MDF if the retention fraction of SN products is low ($f_{\rm ret} \sim 0.3$) – that is, 70 per cent of the metals produced by SNe are directly ejected from the galaxy. The covariance we find between η and $f_{\rm ret}$ in models where both are free implies that ($f_{\rm ret}$, η) = (0.3, 50) is roughly consistent with the mass-loading factor of $\eta \sim 200$ inferred in the fiducial model when $f_{\rm ret} = 1$. Conversely, this covariance implies that to produce a similar MDF with an even smaller mass-loading factor of $\eta \sim 10$ would require a retention factor of only 10 per cent (and also a substantially lower SFE time-scale of $\log_{10}\tau_{\rm SFE} \sim 0.5$).

While the best-fitting MDFs of the fiducial and metal-loading models are both generally consistent with the data (the former more-so than the latter), they do produce qualitatively different MDFs. The metal-loading model predicts a slightly more skewed MDF with a higher metallicity peak and a truncated metal-rich tail. These differences result from the fact that the metal-loading model is always losing a significant fraction of the metals produced, while the fiducial model only experiences significant metal losses once the ISM metallicity approaches its final value.

While discriminating between these two models could be accomplished in theory by acquiring more precise [Fe/H] measurements of stars in the high-metallicity end of the MDF, the similarity of the two model predictions coupled with the paucity of bright stars in Eri II makes doing so in practice implausible. Instead, incorporating independent constraints on the metal-loading factor from observations of local galaxies (e.g. McQuinn et al. 2019) or from hydrodynamic simulations (e.g. Pandya et al. 2021) would prove more fruitful in breaking the degeneracy between η and $f_{\rm ret}$.

4.2.4 *High SFE M=model*

When we force a short SFE time-scale ($\log_{10}\tau_{\rm SFE} \sim 0.4$), we find that the best-fitting MDF is sharply peaked at [Fe/H] ~ -2.4 with roughly exponential tails on either side. The peak of this distribution corresponds to the CC equilibrium Fe-abundance that the model would evolve to in the absence of SN Ia (see WAF17 for derivation):

$$[\mathrm{Fe/H}]^{\rm cc}_{\rm eq} = \log_{10}\left(\frac{y^{\rm cc}_{\rm Fe}}{Z_{\rm Fe,\odot}(1+\eta-r-\tau_{\rm SFE}/\tau_{\rm SFH})}\right). \tag{10}$$

For a galaxy with an exponentially declining SFH, this equilibrium value is approached on the 'harmonic difference time-scale' set by $\tau_{\rm SFH}$ and the gas depletion time-scale $\tau_{\rm dep}$,

$$\tau^{\rm cc}_{\rm Fe,eq} \equiv \left(\tau^{-1}_{\rm dep} - \tau^{-1}_{\rm SFH}\right)^{-1}, \tag{11}$$

where the depletion time-scale is defined to be

$$\tau_{\rm dep} = \frac{\tau_{\rm SFE}}{1+\eta-r}. \tag{12}$$

Equation (11) can be equivalently expressed as

$$\tau^{\rm cc}_{\rm Fe,eq} = \frac{\tau_{\rm SFE}}{1+\eta-r-\tau_{\rm SFE}/\tau_{\rm SFH}}. \tag{13}$$

While both this model and the fiducial model have $[\mathrm{Fe/H}]^{\rm cc}_{\rm eq} \sim -2.4$, the short $\tau_{\rm SFE}$ imposed here results in a substantially smaller $\tau^{\rm cc}_{\rm Fe,eq}$ ($\sim$30 Myr versus $\sim$200 Myr), which is shorter than the 50 Myr minimum time delay for SN Ia. As a result, the model quickly evolves to the equilibrium metallicity where it forms stars until the onset of SN Ia at which point the model evolves to higher metallicity. The sharp decline in the MDF above $[\mathrm{Fe/H}]^{\rm cc}_{\rm eq}$ is due to the short SFH time-scale (0.08 Gyr) inferred for this model – by the time SN Ia begin increasing the metallicity, the rate of star formation is rapidly declining. In contrast, the fiducial model's longer $\tau^{\rm cc}_{\rm Fe,eq}$ is sufficiently long that SNe Ia begin contributing to Fe production before $[\mathrm{Fe/H}]^{\rm cc}_{\rm eq}$ is reached, resulting in a smoother MDF with no sharp peaks. The high SFE model is strongly disfavoured by the BF ($\sim$0.002), and its extremely short $\tau_{\rm SFH}$ appears physically implausible.

4.2.5 *Longer SN Ia delay*

Within the uncertainties of the latent MDF, we find that a model assuming a minimum SN Ia time delay of 0.15 Gyr provides a fit that is roughly as good as that of the fiducial model. With this longer time delay, we infer an SFH time-scale that is slightly larger and a mass-loading factor that is slightly smaller than the fiducial model. The kink in the evolutionary track at [Fe/H] ~ -2.75 corresponds to the onset of SN Ia enrichment (a milder version of the sharp transition found in the High SFE model). In principle one could distinguish the $t_D = 0.05$ and 0.15 Gyr scenarios from the different shapes of the predicted MDFs, but this would require a much larger sample of high-quality stellar metallicities than is currently (or likely ever will be) available in Eri II. Alternatively, these scenarios may be distinguished with sufficiently precise ($\lesssim$0.1 dex) measurements of [α/Fe] as the onset of SN Ia enrichment controls the metallicity of the 'knee' in the [α/Fe]–[Fe/H] distribution (see Section 5.2.1).

4.2.6 *No SN Ia*

We find that a model with no SN Ia enrichment can reproduced Eri II's MDF reasonably well with only slight differences from the MDF of the fiducial model. Like the metal-loading model, this model is most distinguishable in the high-metallicity tail. While this model infers values for the SFE and SFH time-scales and $t_{\rm trunc}$ that are consistent with the fiducial model, it requires a mass-loading factor that is $\sim$2.5 times smaller because the total Fe yield is lower. Unlike the other best-fitting models, this model has an SFH time-scale that is *shorter* than the depletion time-scale $\tau_{\rm dep}$ (equation 12),

0.45 Gyr versus 0.52 Gyr, which is necessary in the absence of SN Ia enrichment to avoid forming an MDF peaked at $[Fe/H]^{cc}_{eq}$. Physically achieving $\tau_{SFH} < \tau_{dep}$ would require the removal of gas from the galaxy by a process not associated with star formation. If this is indeed the case for Eri II then reionization-driven photoevaporation might be responsible for the removal of gas, though this would require additional investigation.

While the BF of this model is marginally larger than the fiducial model, we caution that this alone does not indicate that the no SN Ia model is better. The BF is only informative insofar as the two models are equally likely a priori. The scenario considered here, in which no SN Ia contributed in any part to the Fe enrichment of the stars in our sample, is highly improbable given the expectation that ∼200 SN Ia should have occurred in a galaxy of Eri II's mass. The no SN Ia model could be easily distinguished from the fiducial model with measurements of [α/Fe] ratios, which should remain elevated in the absence of SN Ia enrichment (see Section 5.2.1).

4.2.7 Enhanced SN Ia

Increasing the SN Ia yield by a factor of 10, as an SN Ia rate $\propto Z^{-0.5}$ would imply, results in an MDF with a higher and narrower peak close to the eventual sharp truncation, as well as a secondary low-metallicity peak. The high y^{Ia}_{Fe} forces a high η, which in turn leads to a short depletion time $\tau_{dep} \sim 30$ Myr. As with the high SFE model, this low-metallicity peak is the result of the model evolving to its equilibrium CC Fe abundance (in this case $[Fe/H]^{CC}_{eq} \sim -3.25$) before the commencement of SN Ia at $t_D = 50$ Myr. The enhanced SN Ia model is disfavoured by the BF (∼0.02) and can be easily ruled out if the measurement uncertainties could be reduced to ≲0.3 dex.

The discrepancy on the high-metallicity end of the MDF is alleviated if we allow for $f_{ret} < 1$, which compensates by decreasing the effective SN yield. Indeed, if we set $f_{ret} = 0.1$ for SN Ia but $f_{ret} = 1$ for CCSN, then this model is equivalent to the fiducial model, with direct SN Ia metal loss exactly cancelling the higher yield. However, there is no obvious reason to have a high retention fraction for CCSN but a low retention fraction for SN Ia. We do find that adopting a single $f_{ret} = 0.1$ produces an MDF in better agreement with the fiducial model. While the best-fitting mass-loading factor in this case is similar to that of the fiducial model ($\eta \sim 200$), the inferred SFE time-scale is substantially lower ($\log_{10}\tau_{SFE} \sim 0.7$). If we allow f_{ret} to be free, the model prefers larger retention fractions and mass-loading factors: $f_{ret} \sim 0.6$ and $\eta \sim 700$ (though these parameters, as always, are very degenerate). In all of these permutations, the peak around $[Fe/H]^{CC}_{eq}$ remains.

5 DISCUSSION

5.1 Physical interpretation of the model

Our fiducial model achieves a good match to the observed MDF with physically plausible values of its four evolutionary parameters, $\tau_{SFE} = 27.5$ Gyr, $\tau_{SFH} = 0.39$ Gyr, $t_{trunc} = 1.37$ Gyr, and $\eta = 194$. As previously discussed, a low SFE (large τ_{SFE}) is characteristic of low-M_* dwarfs, and the high η value is consistent with scaling relationships from numerical and analytic models extrapolated to the low mass of Eri II. The *e*-folding time-scale for star formation is consistent with direct estimates of the SFH (Gallart et al. 2021), but the value of t_{trunc} is not independently well constrained by the MDF data.

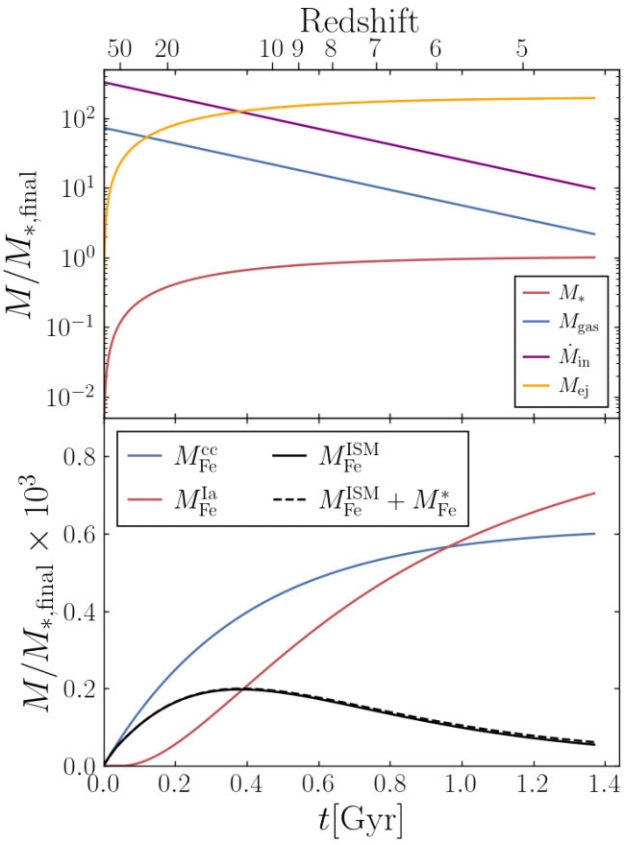

Figure 8. Top: the stellar mass (red), gas mass (blue), infall rate (purple), and cumulative ejected gas mass (orange) of the best-fitting model as a function of time. The star-to-gas ratio is very low at early times but evolves close to unity by the time star formation ceases. At the end of the simulation, the model has lost roughly 100 times its stellar mass in gas outflows. Bottom: the mass of Fe in the ISM (solid black) and the cumulative mass of Fe produced by CCSNe and SN Ia (blue and red, respectively) for the best-fitting model as a function of time. At early times, CCSNe dominate the production of Fe, while at late times the total contribution of CCSNe and SN Ia are roughly equal. While the amount of Fe in the ISM is slowly decreasing for $t > 0.3$ Gyr, the rapidly decreasing gas supply (top panel) results in a monotonically increasing gas-phase metallicity. The mass of Fe in stars is negligible as can be seen from the dashed black line, which shows the combined mass of Fe in both the ISM and long-lived stars.

Fig. 8 elucidates the evolution of the best-fitting fiducial model. Because of the short τ_{SFH}, the model has already formed ∼65 per cent of its stellar mass by $t = 0.4$ Gyr ($z = 11.3$). The gas mass, $M_g = \tau_{SFE}\dot{M}_*$, follows the same exponential decline as the SFH, given the assumption of a constant τ_{SFE}. Through most of the model's evolution the stellar mass fraction $M_*/(M_* + M_g)$ is $\ll 1$, though by the end it has risen to 0.5. However, because the value of η is so high, the mass of gas ejected from the galaxy exceeds the mass remaining in the ISM at all times $t \gtrsim 0.1$ Gyr. The model has vigorous ongoing gas accretion that fuels continuing star formation despite the strong outflow, with an infall rate $\dot{M}_{inf} \approx (\eta - \tau_{SFE}/\tau_{SFH})\dot{M}_* \approx 120\dot{M}_*$ (see equation 4). An exponential SFH requires a non-zero gas mass of $M_g \sim 1.5 \times 10^7$ M$_\odot$ at $t = 0$. In the fiducial model, the mass of gas accreted exceeds this initial mass for $t \gtrsim 0.35$ Gyr and reaches $M_{inf} \sim 2.5 \times 10^7$ M$_\odot$ by $t = t_{trunc}$. This is consistent with the range of gas masses assumed to accrete rapidly onto UFDs by previous chemical evolution studies (e.g. $M_{inf} \sim 1$–5×10^7 M$_\odot$, Vincenzo et al. 2014; Romano et al. 2015; Lacchin et al. 2020; Alexander et al. 2023).

The bottom panel of Fig. 8 tracks the Fe mass budget. In the fiducial model, the total Fe produced by CCSN and SN Ia is nearly equal over the life of the galaxy. However, CCSN enrichment dominates the early evolution, and by late times the enrichment rate from SN Ia greatly exceeds that from CCSN, as one can see by comparing the slopes of the blue and red curves. These conclusions rely on our adopted values of $y_{\rm Fe}^{\rm cc}$ and $y_{\rm Fe}^{\rm Ia}$; as shown in Fig. 7, the MDF can be reasonably well reproduced even in a model with no SN Ia enrichment. For $t > 0.4$ Gyr, the mass of Fe ejected from the galaxy exceeds the mass remaining in the ISM by a substantial factor. The Fe mass in stars is small compared to that in the ISM because the star-to-gas mass ratio is low and because the mean metallicity of stars is always lower than the ISM metallicity.

Although the SFE time-scale is long, the gas depletion time (equation 12) is short because of the high η, $\tau_{\rm dep} \sim 0.14$ Gyr. As discussed by WAF17, obtaining an MDF that turns over rather than peaking sharply requires a rapidly declining SFH so that newly produced metals are deposited in a dwindling gas supply, resulting in high ISM metallicity at late times when only a small number of stars are produced. In the case of the fiducial model, $\tau_{\rm SFE} = 0.39$ Gyr is still significantly longer than $\tau_{\rm dep}$, but it is shorter than the characteristic enrichment time for SN Ia (roughly 1.5 Gyr), so the SN Ia enrichment drives the MDF turnover. In the $y_{\rm Fe}^{\rm Ia} = 0$ model, by contrast, the MDF turnover arises because the depletion time is longer, and with $\tau_{\rm SFH} \sim \tau_{\rm dep}$ the model approaches the leaky box scenario, which was shown to provide a reasonable fit to the Eri II MDF by F22. Our fiducial model is still rather far from this limit.

We can summarize the physical properties of the fiducial model as follows. It begins with an initial gas mass $M_g \sim 1.5 \times 10^7$ M$_\odot$ and accretes gas vigorously but at an exponentially declining rate. Only a small fraction of the $\sim$2.5 $\times$ 10^7 M$_\odot$ of accreted gas forms into stars because the SFE is low and because feedback from star formation drives ISM gas out of the galaxy's shallow potential well with a high mass-loading factor $\eta \sim 200$. Fe enrichment is dominated by CCSN at early times and by SN Ia at later times, with the two channels producing similar total amounts of Fe over the life of the galaxy. However, more than 90 per cent of the Fe produced by the stars is ejected from the galaxy. This low metal retention is the main reason for the galaxy's low final metallicity, not the truncation of star formation. The turnover in the MDF arises because Fe from SN Ia is deposited in a dwindling gas supply, enabling a small fraction of stars to form at relatively high [Fe/H]. The exponentially declining SFH arises because gas accretion does not keep up with gas losses from the feedback-induced galactic wind. Star formation ceases abruptly at $t = t_{\rm trunc} \sim 1.4$ Gyr ($z \sim 4.3$), presumably because reionization evaporates the galaxy's remaining gas supply.

5.2 Additional model predictions

5.2.1 Predictions of [Mg/Fe]

While we do not consider [Mg/Fe] in our fit (there being presently no stars in Eri II with [α/Fe] measurements of any kind), we can use our model to make predictions of the [Mg/Fe] evolution in Eri II that next-generation spectroscopic facilities will soon be able to test (e.g. Sandford, Weisz & Ting 2020). In principle, measurements of [Mg/Fe] for even a few stars in our sample should provide tighter constraints on our posteriors.

In Fig. 9 (top), we display the distribution of stars in [α/Fe]–[Fe/H] space that is compatible with our fiducial Eri II model (grey-scale histogram). This distribution is generated by sampling 60 stars from each of the 1000 randomly drawn posterior predictions included in Fig. 4. Evolutionary tracks of these models are also included here as thin red lines. Red circles depict 10 Myr snapshots of the best-fitting model, where the size of the marker is proportional to the relative SFR at that time; time-steps corresponding to 10 Myr, 100 Myr, and 1 Gyr are outlined in black.

As described in the Section 3.1, the low-metallicity plateau of [Mg/Fe] ~ 0.5 is produced by design given our adopted CC Mg and Fe yields. The turnover or 'knee' in the [Mg/Fe]–[Fe/H] distribution occurs at [Fe/H] ~ -3.0, which is the metallicity of the model at $t = 50$ Myr when SN Ia begin to contribute to Fe production. The SN Ia Fe yield was set to $y_{\rm Fe}^{\rm Ia} = 0.0012$ such that an MW disc-like model evolves to [Fe/H] $\approx$ [Mg/Fe] ≈ 0 at late times. Unsurprisingly, the evolution of a UFD-like model presented here only evolves to [Fe/H] ~ -1.75, but it reaches subsolar Mg abundances of [Mg/Fe] ~ -0.2 because of the short $\tau_{\rm SFH}$. [Mg/Fe] measurements in UFDs are sparse and uncertain, especially for [Fe/H] $\lesssim -3$, but our predictions are generally consistent with observations (e.g. Simon 2019, and references therein).

Though the locus of possible [Mg/Fe]–[Fe/H] falls relatively tightly around the best-fitting fiducial model, the spread in the posterior predictions is substantial both in the location of the knee and the final [α/Fe]. This suggests, similar to the comparison of alternative models in Fig. 7, that the more metal-rich stars in Eri II hold increased constraining power. Fortunately, these are also the stars for which spectroscopic measurements should be (comparatively) easier. That being said, measuring [Mg/Fe] in stars with [Fe/H] < -3.0 will provide valuable constraints on the CC SN yields that determine the high-[Mg/Fe] plateau.

The constraining power of [Mg/Fe] measurements is further exemplified in the bottom panel of Fig. 9, where the [Mg/Fe]–[Fe/H] evolution of the alternative models are compared to that of the fiducial model. The no SN Ia model (green) is easily distinguishable from the fiducial model (black) because without SN Ia enrichment [Mg/Fe] remains elevated. Meanwhile the enhanced SN Ia model (yellow) is distinguishable for the opposite reason because the extra SN Ia enrichment drives [Mg/Fe] lower faster. The low SFE of the constant SFR model (purple) leads to SN Ia decreasing [Mg/Fe] at lower [Mg/Fe] than other models, while its low mass-loading factor means more of the CCSN products produced early are retained, keeping [Mg/Fe] from decreasing as steeply. In the high SFE model (pink), [Fe/H] evolves much more rapidly so the knee occurs at higher metallicity, but given the short $\tau_{\rm SFH}$ inferred for this model, few stars are formed at lower [Mg/Fe]. The differences predicted by the longer SN Ia delay model (brown) and the metal-loading model (orange) compared to the fiducial model are smaller. The longer time delay before SN Ia start shifts the [Mg/Fe]–[Fe/H] track to higher metallicities, while the direct loss of metals makes SN Ia slightly less effective at decreasing [Mg/Fe] at late times. Once again, precise abundance measurements of stars at the high-metallicity end will provide the best opportunity to discriminate between these models.

5.2.2 Ultra metal-poor stars

Our hierarchical Bayesian framework enables us to recover the posterior distribution of the latent [Fe/H] for each star in our sample. We caution, however, that these inferred values are influenced by the model MDF and represent the 'true' [Fe/H] of each star only insofar as the model represents the true MDF of Eri II. Further, because a truncation of the MDF and [Fe/H] priors below [Fe/H] < -4 is imposed by the limitations of the stellar grid used in the CaHK measurements, we cannot recover the metallicity of a star to

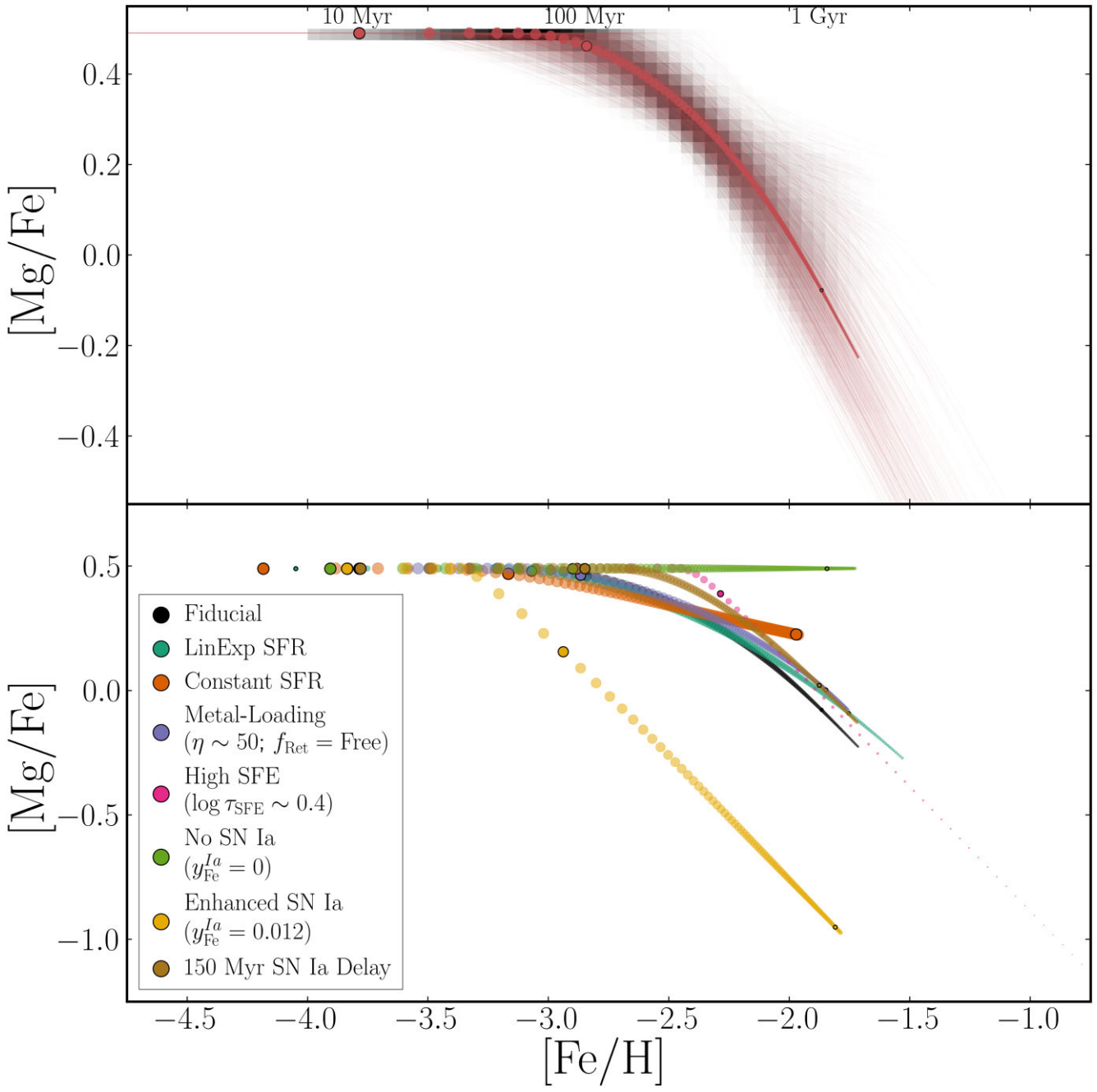

Figure 9. Top: [Mg/Fe]–[Fe/H] distribution of stars (grey-scale histogram) predicted by models sampled from our posterior distribution (thin red lines). The evolution of the best-fitting fiducial model in steps of 10 Myr is depicted in red circles; the size of the marker is proportional to the SFR at each step. Bottom: the evolution of the best-fitting alternative models (coloured circles) compared to the fiducial model's evolution (black circles) following the same plotting convention as the top panel. While many of the alternative models produce MDFs similar to the fiducial model, they predict quite distinct [Mg/Fe]–[Fe/H] distributions.

be more metal-poor than [Fe/H] < -4 even if such a star was in our sample. That being said, our framework does allow us to compare the relative probability that each star in our sample was drawn from the untruncated MDF and the redistributed metal-poor tail of the MDF (see Fig. 2). By doing this for the entire posterior sample, we can infer the probability that each star is truly an ultra metal-poor (UMP) star with [Fe/H] < -4.

Fig. 10 shows the probability of being an UMP star for the 10 highest probability stars. We find that the posterior distribution on P([Fe/H] < -4) is consistent with zero for every star, strongly disfavouring the presence of any UMP star in our sample. This result suggests that no pre-enrichment of Eri II's gas supply or metallicity floor is necessary to explain the dearth of UMP stars, though a larger sample of stars is necessary to conclusively rule out these scenarios. We place 95 per cent upper limits on the ultra-metal poor probability of each star and find 10 stars with upper limits greater than 15 per cent. Stars 11 and 21 have upper limits greater than 40 per cent and were previously identified as extremely metal-poor ([Fe/H] $<$

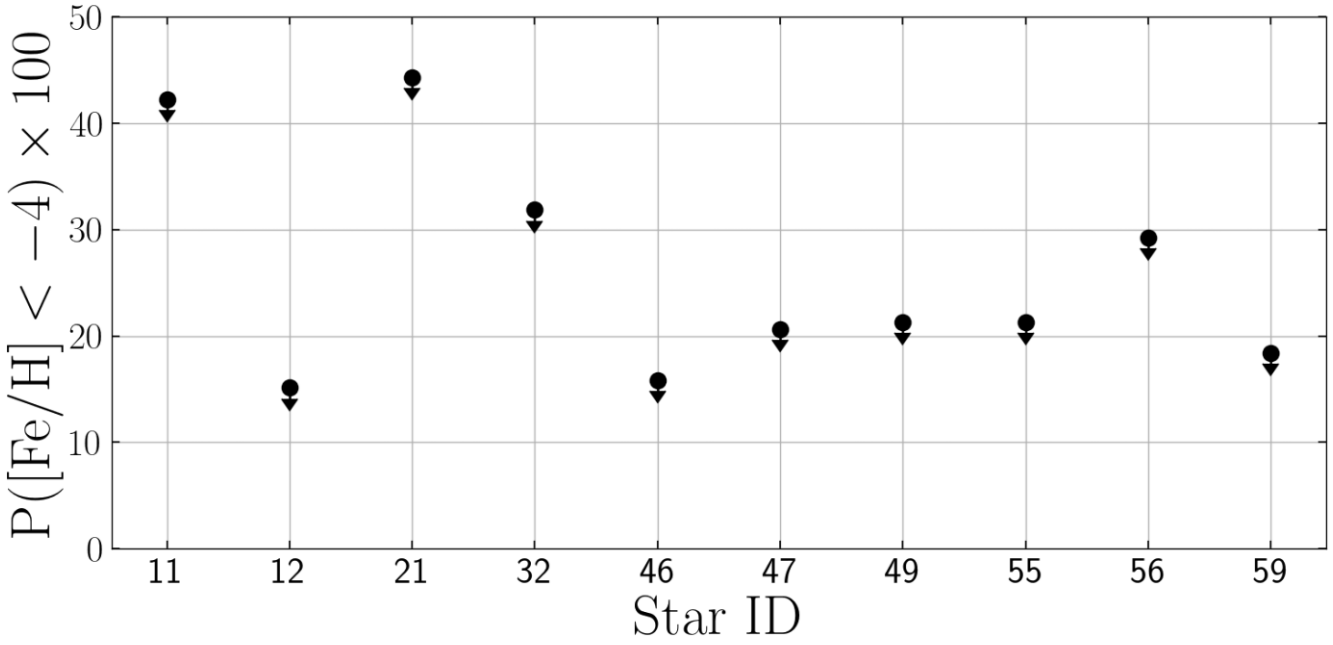

Figure 10. 95 per cent upper limits on the inferred probability of metallicities below [Fe/H] < -4 for the highest probability stars in our sample. The remaining 50 stars have probabilities <15 per cent. Stars 11 and 21 were previously identified as extremely metal-poor ([Fe/H] < -3) candidates by F22.

-3) candidates by F22. Searches for UMP stars in Eri II should prioritize this subset of our sample for spectroscopic follow-up in order to confirm their true metallicity.

5.3 Potential limitations of a one-zone model

The analytic solutions employed in our analysis require several idealizations, such as constant values of $\tau_{\rm SFE}$ and η. The most important idealization is the one-zone framework itself, that is, the assumption that the star-forming ISM can be treated as a single, fully mixed gas reservoir with abundances that evolve in time but do not vary with position. Our key finding is that the fiducial model reproduces the observed MDF of Eri II with parameter values that appear plausible on empirical and theoretical grounds. More complicated models for the chemical evolution of Eri II are certainly possible, but they are not required by the observed MDF.

The sharpest conclusion from our modelling is that the observed MDF implies a rapidly declining SFH, with $\tau_{\rm SFH} \sim 0.4$ Gyr, in addition to an eventual truncation. This conclusion is driven by the turnover and slow decline of the MDF, as opposed to the high peak and rapid cutoff predicted for models with roughly constant SFR (WAF17). As discussed in Section 4.2, clearly ruling out this model would require more precise [Fe/H] values for the highest metallicity stars in Eri II, but the predicted MDF shape for a constant SFR clearly differs from that inferred in most studies of low-luminosity dwarfs. Returning to Fig. 4, we note that the portion of the MDF beyond the maximum at [Fe/H] ~ -2.25 is populated by by stars whose posterior p([Fe/H]) peaks at higher [Fe/H], not by the long tails of stars whose most probably [Fe/H] is lower. Thus, there is no indication in the data that the smooth turnover of the MDF (as opposed to a sharp cut-off) is caused by observational scatter.

There are two ways in which departures from a one-zone model could explain a turnover in the MDF without a rapidly declining SFH or otherwise bias our results: (1) spatial metallicity gradients and (2) stochastic enrichment events. We discuss these scenarios below, but note that either of these would require additional degrees of freedom to model. If it remains consistent with future data, the parsimony of the four-parameter one-zone model is an argument in its favour.

5.3.1 *Spatial gradients*

Many, though not all, dwarf galaxies are known to host mild radial stellar metallicity gradients of $\nabla_{\rm [Fe/H]} \sim -0.1$ dex/$r_{\rm h}$ (see Taibi et al. 2022, and references therein). The presence of a metallicity gradient in Eri II could impact our results in one of two ways. Our sample may be biased to higher metallicity because our CaHK measurements only include stars within $\sim$1 $r_{\rm h}$ thereby missing the most metal-poor stars at large radii. Alternatively, the shape of Eri II's MDF may be altered by the inclusion of stars at a range of radii that do not share identical chemical enrichment histories, thus violating the assumption of a one-zone chemical evolution model.

In most cases, the metallicity gradients of dwarf galaxies are thought to be primarily generated by feedback-driven outflows, which heat stellar orbits and preferentially drive outward migration of old stars (El-Badry et al. 2016). Because the oldest stars are also likely to be the most metal-poor, this migration can create a negative stellar metallicity gradient with more metal-rich stars at small radii and more metal-poor stars at large radii. While El-Badry et al. (2016) find feedback-driven stellar migration to be more pronounced for low-mass galaxies in a slightly larger mass regime ($M_* \sim 10^{7\text{–}9.6}$),[6] we cannot entirely rule out the possibility that our sample of stars in Eri II has been impacted by radial migration.

Alternatively, radial metallicity gradients may be indicative of radial gradients in galactic physics. For example, if the outflow mass-loading increased with radius or the SFE decreased with radius, then the central regions of the galaxy could evolve to higher [Fe/H] than

[6]Specifically, El-Badry et al. (2016) find that the higher dark matter fractions and lower SFE of less massive galaxies leads to smaller fluctuations in the galactic potential and therefore weaker coupling between feedback-driven outflows and stellar kinematics.

the outer regions. In principle, this could produce a small fraction of stars with [Fe/H] beyond the peak of the MDF, creating the turnover we see in Eri II's MDF without needing to invoke an exponentially declining SFH. We have not experimented with such models, but with freedom to choose the density profile and $\eta(r)$ or $\tau_{\rm SFE}(r)$ we expect one could produce a range of MDF shapes. In chemical evolution studies of more massive galaxies like the MW, radial variations in model parameters is indeed important and has motivated the replacement of the single one-zone model with a series of concentric one-zone models, each representing a radial annulus of the galaxy (e.g. Matteucci & Francois 1989; Schönrich & Binney 2009; Minchev, Chiappini & Martig 2013; Johnson et al. 2021; Sharma, Hayden & Bland-Hawthorn 2021). However, such effects are likely to be much less important for UFDs like Eri II, which formed the bulk of their stars on very short time-scales and very small spatial scales.

So far, only two studies, Martínez-Vázquez et al. (2021) and F22, have attempted to measure a stellar radial metallicity gradient in Eri II. Using a sample of 67 RR Lyrae stars, Martínez-Vázquez et al. (2021) measured a strong negative metallicity gradient of -0.46 dex/$r_{\rm h}$ in the inner half-light radius of Eri II. However, a gradient of this magnitude is highly unusual for an isolated dwarf galaxy of Eri II's mass and is more characteristic of dwarf galaxies known to have experienced a past merger event (e.g. Sextans, Andromeda II, Phoenix, and NGC 6822; Taibi et al. 2022). Moreover, F22, which provides the observational basis for our analysis, found no evidence for a spatial trend in stellar [Fe/H] within one half-light radius where the gradient was reported to be strongest by Martínez-Vázquez et al. (2021). The origin of this discrepancy remains uncertain and merits future investigation. Nevertheless, because no radial metallicity gradient exists within our sample, we do not believe the shape of our MDF to be substantially altered by the presence of spatial gradients in Eri II.

It is still possible that we are biased by our centrally concentrated sample, which may not include old, metal-poor stars that formed or migrated beyond the inner half-light radius. A more spatially extended survey of stellar metallicities in Eri II is necessary in order to rule this possibility out. If it turns out that our current sample is missing a sizeable population of metal-poor stars, then the SFE or SFH time-scale we infer may be biased high. A more spatially extended survey of stellar metallicities in Eri II is necessary in order to quantify the magnitude of the bias or rule this possibility out.

5.3.2 Stochastic supernova enrichment

A second possible departure from our model assumptions is Poisson sampling of the SN population. For $M_* \sim 2 \times 10^5$ M$_\odot$ the number of CCSN is ∼2000 and the number of SN Ia is ∼200. If the reservoir is fully mixed, as appears to be a reasonable assumption for ancient dwarf galaxies (see Escala et al. 2018), then Poisson fluctuations would produce only minor variations in the enrichment history, at least at the high-metallicity end of the MDF. However, if the galaxy is divided into smaller zones that do not efficiently share metals with each other then the number of SNe that contribute to the composition of any given star is smaller. In this scenario, the high-metallicity tail of the MDF could be populated by stars that happened to be enriched by unusually large numbers of SNe – most likely SN Ia because of their smaller numbers and larger Fe yield per SN, though stochastic sampling of the IMF at late times when the SFR is low may also contribute to fluctuations in the number of CCSNe. In principle this scenario could be tested by measuring stochastic fluctuations in element ratios, following the arguments presented by Griffith et al. (2023). While stochastic sampling may be a small effect in this study of Eri II, it is likely to be more important in lower mass UFDs where the total number of CCSN and SN Ia may be smaller and in analyses that involve additional element ratios (e.g. Alexander et al. 2023).

5.4 Comparison to Johnson et al. (2023a)

Although the formulation is quite different, our method has features in common with the recently proposed method of Johnson et al. (2023b, hereafter J23a), which also fits dwarf galaxy abundance data with one-zone chemical evolution models. The J23a method considers the probability that each star can be associated with each point on a model evolutionary track. Weighting these probabilities by the model SFR enforces a good match to the MDF of the data set. Our method works directly from the MDF, though the treatment of measured P([Fe/H]|CaHK) as a prior on the latent P([Fe/H]′) of each star makes the calculation resemble the likelihood calculation of J23a. J23a consider data with both [α/Fe] and [Fe/H] measurements, and the [α/Fe] turnover provides leverage on the model time-scales given the DTD of SN Ia enrichment. For Eri II we have been able to derive surprisingly strong constraints from P([Fe/H]) alone, though we are aided by the turnover form of the MDF and by the known early truncation of star formation.

We suspect, but have not yet tested, that the two methods would give similar results from equivalent input data. We use the WAF17 analytic solutions while J23a use numerical computations from `VICE` (Johnson & Weinberg 2020), but in principle either method could be implemented using analytic or numerical chemical evolution calculations. Our method could be generalized to model a joint P([α/Fe], [Fe/H]) distribution, but the J23a method may be simpler to implement when multiple observables per star are included. Conversely, our approach may be better adapted to complex non-Gaussian [Fe/H] uncertainties like those derived from CaHK photometry. Further work is merited to understand the consistency of these approaches and their relative strengths for different classes of observational data.

6 CONCLUSION

In this work, we use an analytic one-zone galactic chemical evolution model to fit the CaHK MDF of Eri II in a hierarchical Bayesian framework that appropriately accounts for non-Gaussian measurement uncertainties. Our fiducial model achieves a good match to the observed MDF from which we infer reasonable constraints on Eri II's SFH ($\tau_{\rm SFH} = 0.39\pm^{0.18}_{0.13}$ Gyr), SFE ($\tau_{\rm SFE} = 27.56\pm^{25.14}_{12.92}$ Gyr), and mass-loading factor ($\eta = 194.53\pm^{33.37}_{42.67}$). These results are consistent with expectations of both low SFE and high η in low-mass galaxies and with direct estimates of Eri II's SFH from deep photometric data.

Our best-fitting fiducial model paints the following picture of Eri II's evolution. When star formation began, Eri II had an initial gas mass of $\sim 10^7$ M$_\odot$ and continued to accrete gas vigorously but at an exponentially declining rate. Because of its low SFE and the presence of strong stellar feedback which drives ISM gas out of its shallow potential well, only a small fraction of the accreted gas is converted into stars. The production of Fe is dominated at early times by CCSNe and at late times by SN Ia, though feedback-induced galactic winds remove >90 per cent of all Fe from the galaxy, resulting in Eri II's low final metallicity. Gas loss from these large outflows outpaces gas accretion, resulting in an exponentially declining SFH that truncates at ∼1.4 Gyr – likely as a result of reionization evaporating its remaining gas supply.

In addition to our fiducial model, we consider several alternative models to build physical intuition and test specific formation scenarios (e.g. a constant SFR). These models, by-and-large, yield less natural fits to Eri II's MDF compared to the fiducial model, though in some cases they remain statistically acceptable because of the uncertainties of the stellar [Fe/H] measurements. Additional investigation is required to evaluate the role that spatial variation and stochastic SN enrichment may play in Eri II's MDF. Similarly, given its low mass and early star formation, a more physically motivated treatment of reionization is warranted. It is encouraging that the stellar MDF alone gives informative constraints on the evolution of Eri II within the framework of the fiducial model.

Regarding future observations of Eri II and other UFDs, we stress the importance of acquiring precise spectroscopic abundances of not just the lowest metallicity stars, but also – and especially – stars at the high-metallicity end of the MDF. The metallicities and element abundance ratios of these stars will provide some of the strongest constraints on the inferred evolution of their host galaxies.

ACKNOWLEDGEMENTS

We thank the anonymous referee for constructive comments that helped improve the paper. We thank Ellie Abrahams, Ani Chiti, Alex Ji, James Johnson, Andrey Kravtsov, and Alessandro Savino for insightful discussion on this work. NRS is grateful for the hospitality of the Ohio State University Department of Astronomy during the conclusion of this work. NRS and SFW acknowledge support from the National Science Foundation Graduate Research Fellowship Program under grants DGE 1752814 and DGE 2146752. SWF also acknowledges support from the Paul & Daisy Soros Fellowship. NRS, DRW, and SWF acknowledge support from HST-GO-15901, HST-AR-16159, HST-GO-16226, and JWST DD-ERS-1334 from the Space Telescope Science Institute, which is operated by AURA, Inc., under the National Aeronautics and Space Administration contract NAS5-26555. DHW acknowledges the support and hospitality of the Miller Institute for Basic Research during the initiation of this work and the support of National Science Foundation grant AST-19009841. The computations in this paper were partially run on the Savio computational cluster resource provided by the Berkeley Research Computing Program at the University of California, Berkeley.

Software: ASTROPY (Astropy Collaboration 2013, 2018, 2022), CORNER (Foreman-Mackey 2016), MATPLOTLIB (Hunter 2007), NUMPY (van der Walt, Colbert & Varoquaux 2011; Harris et al. 2020), PANDAS (McKinney 2010; Reback et al. 2022), POCOMC (Karamanis et al. 2022a, b), and SCIPY (Virtanen et al. 2020).

DATA AVAILABILITY

The data and code underlying this article are available in a GITHUB repository, at https://github.com/NathanSandford/ChemWAF.

REFERENCES

Planck Collaboration 2020, A&A, 641, A6
Alexander R. K., Vincenzo F., Ji A. P., Richstein H., Jordan C. J., Gibson B. K., 2023, MNRAS, 522, 5415
Andrews B. H., Weinberg D. H., Schönrich R., Johnson J. A., 2017, ApJ, 835, 224
Asplund M., Grevesse N., Sauval A. J., Scott P., 2009, ARA&A, 47, 481
Astropy Collaboration, 2013, A&A, 558, A33
Astropy Collaboration, 2018, AJ, 156, 123
Astropy Collaboration, 2022, ApJ, 935, 167
Battaglia G., Taibi S., Thomas G. F., Fritz T. K., 2022, A&A, 657, A54
Bechtol K. et al., 2015, ApJ, 807, 50
Behroozi P. S., Wechsler R. H., Conroy C., 2013, ApJ, 762, L31
Benson A. J., Bower R. G., Frenk C. S., Lacey C. G., Baugh C. M., Cole S., 2003, ApJ, 599, 38
Chevalier R. A., Clegg A. W., 1985, Nature, 317, 44
Chisholm J., Tremonti C. A., Leitherer C., Chen Y., 2017, MNRAS, 469, 4831
Choi J., Dotter A., Conroy C., Cantiello M., Paxton B., Johnson B. D., 2016, ApJ, 823, 102
Conroy C. et al., 2022, Birth of the Galactic Disk Revealed by the H3 Survey, doi:10.48550/arXiv.2204.02989
Crnojević D., Sand D. J., Zaritsky D., Spekkens K., Willman B., Hargis J. R., 2016, ApJ, 824, L14
Davé R., Katz N., Oppenheimer B. D., Kollmeier J. A., Weinberg D. H., 2013, MNRAS, 434, 2645
Dotter A., 2016, ApJS, 222, 8
Eggen N. R., Scarlata C., Skillman E., Jaskot A., 2021, ApJ 912 12
El-Badry K., Wetzel A., Geha M., Hopkins P. F., Kereš D., Chan T. K., Faucher-Giguère C.-A., 2016, ApJ, 820, 131
Emerick A., Bryan G. L., Mac Low M.-M., 2019, MNRAS, 482, 1304
Escala I. et al., 2018, MNRAS, 474, 2194
Finlator K., Davé R., 2008, MNRAS, 385, 2181
Foreman-Mackey D., 2016, J. Open Source Softw., 1, 24
Fu S. W. et al., 2022, ApJ, 925, 6
Gallart C. et al., 2021, ApJ, 909, 192
Griffith E. J., Sukhbold T., Weinberg D. H., Johnson J. A., Johnson J. W., Vincenzo F., 2021, ApJ, 921, 73
Griffith E. J., Johnson J. A., Weinberg D. H., Ilyin I., Johnson J. W., Rodriguez-Martinez R., Strassmeier K. G., 2023, ApJ, 944, 47
Harris C. R. et al., 2020, Nature, 585, 357
Hopkins P. F., Quataert E., Murray N., 2012, MNRAS, 421, 3522
Hopkins P. F., Kereš D., Oñorbe J., Faucher-Giguère C.-A., Quataert E., Murray N., Bullock J. S., 2014, MNRAS, 445, 581
Hopkins P. F. et al., 2018, MNRAS, 480, 800
Howell D. A. et al., 2009, ApJ, 691, 661
Hunter J. D., 2007, Comput. Sci. Eng., 9, 90
Johnson J. W., Weinberg D. H., 2020, MNRAS, 498, 1364
Johnson J. W. et al., 2021, MNRAS, 508, 4484
Johnson J. W. et al., 2023a, MNRAS, 526, 5084
Johnson J. W., Kochanek C. S., Stanek K. Z., 2023b, MNRAS, 526, 5911
Karamanis M., Nabergoj D., Beutler F., Peacock J., Seljak U., 2022a, J. Open Source Softw., 7, 4634
Karamanis M., Beutler F., Peacock J. A., Nabergoj D., Seljak U., 2022b, MNRAS, 516, 1644
Kirby E. N., Lanfranchi G. A., Simon J. D., Cohen J. G., Guhathakurta P., 2011, ApJ, 727, 78
Koposov S. E., Belokurov V., Torrealba G., Evans N. W., 2015, ApJ, 805, 130
Kroupa P., 2001, MNRAS, 322, 231
Lacchin E., Matteucci F., Vincenzo F., Palla M., 2020, MNRAS, 495, 3276
Lanfranchi G. A., Matteucci F., 2004, MNRAS, 351, 1338
Lanfranchi G. A., Matteucci F., 2007, A&A, 468, 927
Lanfranchi G. A., Matteucci F., 2010, A&A, 512, A85
Lanfranchi G. A., Matteucci F., Cescutti G., 2006, A&A, 453, 67
Leroy A. K., Walter F., Brinks E., Bigiel F., de Blok W. J. G., Madore B., Thornley M. D., 2008, AJ, 136, 2782
Li T. S. et al., 2017, ApJ, 838, 8
Maoz D., Graur O., 2017, ApJ, 848, 25
Maoz D., Mannucci F., Brandt T. D., 2012, MNRAS, 426, 3282
Martínez-Vázquez C. E. et al., 2021, MNRAS, 508, 1064
Matteucci F., Francois P., 1989, MNRAS, 239, 885
McKinney W., 2010, in van der Walt S., Millman J.eds, Proceedings of the 9th Python in Science Conference. p. 56
McQuinn Kristen. B. W., van Zee L., Skillman E. D., 2019, ApJ, 886, 74
Minchev I., Chiappini C., Martig M., 2013, A&A, 558, A9
Mitchell P. D., Schaye J., Bower R. G., Crain R. A., 2020, MNRAS, 494, 3971

Muratov A. L., Kereš D., Faucher-Giguère C.-A., Hopkins P. F., Quataert E., Murray N., 2015, MNRAS, 454, 2691
Murray N., Quataert E., Thompson T. A., 2005, ApJ, 618, 569
Murray N., Quataert E., Thompson T. A., 2010, ApJ, 709, 191
Pandya V. et al., 2021, MNRAS, 508, 2979
Peeples M. S., Shankar F., 2011, MNRAS, 417, 2962
Reback J. et al., 2022, Pandas-Dev/Pandas: Pandas 1.4.3., Zenodo, Accessed 24 January 2023
Rodríguez Ó., Maoz D., Nakar E., 2023, ApJ, 955, 71
Romano D., Bellazzini M., Starkenburg E., Leaman R., 2015, MNRAS, 446, 4220
Sandford N. R., Weisz D. R., Ting Y.-S., 2020, ApJS, 249, 24
Schönrich R., Binney J., 2009, MNRAS, 396, 203
Sharma S., Hayden M. R., Bland-Hawthorn J., 2021, MNRAS, 507, 5882
Simon J. D., 2019, ARA&A, 57, 375
Simon J. D. et al., 2021, ApJ, 908, 18
Somerville R. S., Davé R., 2015, ARA&A, 53, 51
Taibi S., Battaglia G., Leaman R., Brooks A., Riggs C., Munshi F., Revaz Y., Jablonka P., 2022, A&A, 665, A92
Vincenzo F., Matteucci F., Vattakunnel S., Lanfranchi G. A., 2014, MNRAS, 441, 2815
Virtanen P. et al., 2020, Nat. Methods, 17, 261
van der Walt S., Colbert S. C., Varoquaux G., 2011, Comput. Sci. Eng., 13, 22
Weinberg D. H., Andrews B. H., Freudenburg J., 2017, ApJ, 837, 183
Weinberg D. H., Griffith E. J., Johnson J. W., Thompson T. A., 2023, preprint (arXiv:2309.05719)
Zoutendijk S. L. et al., 2020, A&A, 635, A107
Zoutendijk S. L., Brinchmann J., Bouché N. F., den Brok M., Krajnović D., Kuijken K., Maseda M. V., Schaye J., 2021, A&A, 651, A80

APPENDIX A: ISOLATING PARAMETER INFLUENCES ON THE MODEL MDF

The ability of Eri II's MDF to constrain the model parameters can be understood by investigating how each parameter changes the predicted model MDF. In Fig. A1, we show how the MDF changes as we increase and decrease each parameter from the best-fitting fiducial model. With all other parameters held fixed, increasing $\log_{10}\tau_{\rm SFE}$ results in a higher CC equilibrium abundance $[{\rm Fe/H}]^{\rm cc}_{\rm eq}$ and a longer time-scale CC equilibrium time-scale $\tau^{\rm cc}_{\rm Fe,eq}$ (equations 10–12). This leads to a broader MDF with a more extended low-metallicity tail (top-left panel). In the SFE regime of Eri II, changing $\log_{10}\tau_{\rm SFE}$ does not strongly change the location of the MDFs peak. Increasing $\tau_{\rm SFH}$ has roughly the opposite effect of $\log_{10}\tau_{\rm SFE}$, decreasing both $[{\rm Fe/H}]^{\rm cc}_{\rm eq}$ and $\tau^{\rm cc}_{\rm Fe,eq}$ and resulting in a narrower MDF with a smaller low-metallicity tail (top-right panel). While the similarities in impact between $\tau_{\rm SFH}$ and $\tau_{\rm SFE}$ lead to the covariance in their posteriors seen in Fig. 3, they are not fully degenerate. Unlike for $\tau_{\rm SFE}$, decreasing $\tau_{\rm SFH}$ shifts the peak of the MDF to lower metallicity. Furthermore, a more extended SFH leads to an MDF that is more sharply truncated at the high-metallicity end by the abrupt end to star formation at $t_{\rm trunc}$. In comparison, the effect of η on the shape of the MDF is more distinct (bottom-right panel). Increasing the mass-loading factor removes more metals from the galaxy, slowing the rate of enrichment and decreasing the final metallicity that the system evolves to. Higher outflows result in a narrower MDF with a lower metallicity peak and maximum [Fe/H]. Changing η, however, has little impact on the low-metallicity tail of the MDF ([Fe/H] < −3.5). The direct impact

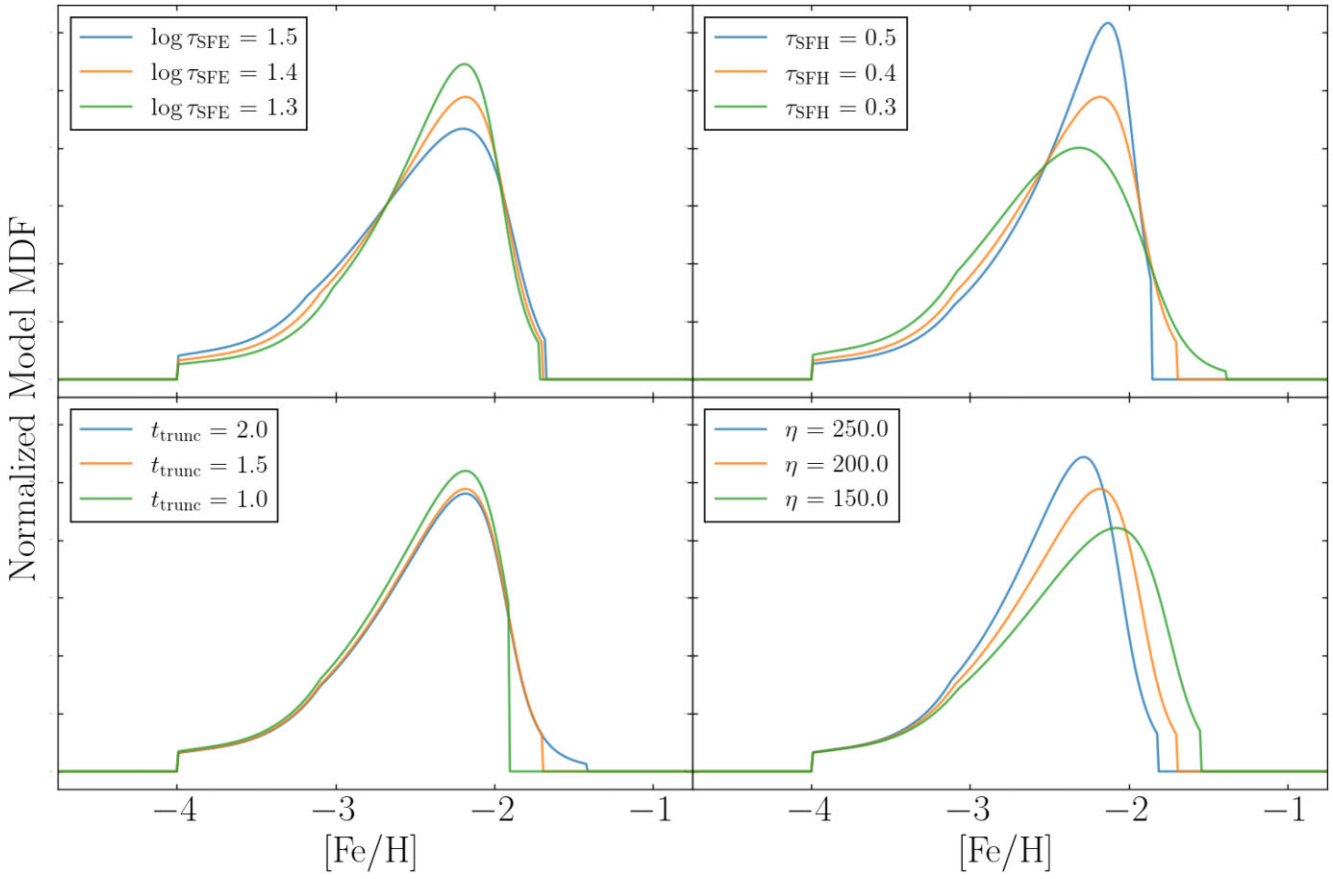

Figure A1. Predicted MDF of the fiducial model as each of the free model parameters is individually increased (blue) and decreased (green) from the approximate best-fitting value (orange).

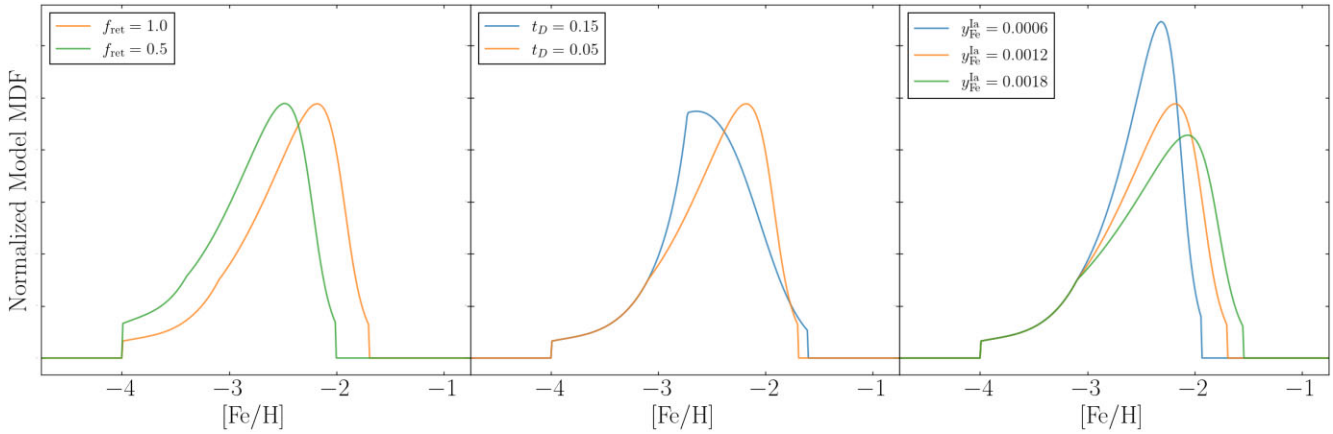

Figure A2. Predicted MDF of the best-fitting fiducial model (orange) compared to the predicted MDF when different values of $f_{\rm ret}$, t_D, and $y_{\rm Fe}^{\rm Ia}$ are adopted.

of $t_{\rm trunc}$ itself is more subtle than the aforementioned parameters, because it is only responsible for the truncation of the MDF at higher metallicities (and the induced re-normalization; bottom-left panel). In our models of Eri II, $\tau_{\rm SFH}$ is sufficiently short that the SFR is quite low at the time of truncation, and thus the portion of the MDF that is truncated is small. It is therefore understandable that $t_{\rm trunc}$ is prior dominated in our fits; there is no clear signature in Eri II's MDF indicating the abrupt cessation of star formation.

In Fig. A2, we illustrate how varying a handful of model parameters that were held fixed in the fiducial model, including $f_{\rm ret}$, t_D, and $y_{\rm Fe}^{\rm Ia}$, influences the predicted MDF in Fig. A2. Reducing $f_{\rm ret}$ effectively reduces the yield of all SNe, which shifts the entire MDF to lower metallicities (left panel). A factor of two reduction as shown here results in a 0.3 dex shift to lower metallicity. When t_D is increased, SN Ia contribute less to the enrichment of the system overall and especially at early times, resulting in an MDF with a lower-metallicity peak (middle panel). The shape of the MDF below [Fe/H] < -2.5 when $t_D = 0.15$ Gyr is due to the model approaching the CC equilibrium metallicity, which it does on a time-scale roughly equivalent to the minimum SN Ia time delay ($\tau_{\rm Fe,eq}^{\rm cc} \sim t_D$). Increasing $y_{\rm Fe}^{\rm Ia}$ has much the same effect as decreasing η. Large SN Ia yields drives the system to higher metallicity for $t > t_D$, resulting in broader, more metal-rich MDFs. This degeneracy with η explains why the enhanced SN Ia model required such large mass-loading factors to reproduce the Eri II MDF.

APPENDIX B: IMPACTS OF INCREASING SAMPLE SIZE AND MEASUREMENT PRECISION

To evaluate the degree to which increasing the number and precision of [Fe/H] measurements would improve model discrimination, we perform a series of mock fits on simulated MDFs. Specifically, we create two mock data sets of 60 and 120 stars drawn from the fiducial model's latent MDF. We fit the MDFs of each sample with each of the models as before adopting 0.3 dex Gaussian uncertainties for the stellar [Fe/H]. These fits are then repeated assuming more precise [Fe/H] measurements with Gaussian uncertainties of 0.1 dex. In each case, we compare the Bayesian evidence of the fiducial model to that of the alternative models and calculate the corresponding BF as described in Section 4.2.

In Table B1, we present the BF of each model relative to the fiducial model for each of the mock fits. As expected, the hHigh

Table B1. The estimated BF relative to the fiducial model from fits to mock samples drawn from the fiducial model's latent MDF. We include the BFs from the fits to real data presented in Table 2 for easy reference.

Model	$N_{\rm star}$	$\sigma_{\rm [Fe/H]}$	BF
Linear-exponential SFR	60	Obs.	3.099
	60	0.3	0.989
	60	0.1	0.156
	120	0.3	1.336
	120	0.1	0.264
Constant SFR	60	Obs.	0.232
	60	0.3	0.002
	60	0.1	<0.001
	120	0.3	<0.001
	120	0.1	<0.001
Metal loading	60	Obs.	0.711
	60	0.3	0.173
	60	0.1	0.568
	120	0.3	0.045
	120	0.1	0.284
High SFE	60	Obs.	0.002
	60	0.3	0.008
	60	0.1	<0.001
	120	0.3	0.015
	120	0.1	<0.001
Longer SN Ia delay	60	Obs.	1.018
	60	0.3	0.775
	60	0.1	0.935
	120	0.3	0.120
	120	0.1	0.456
No SN Ia	60	Obs.	2.239
	60	0.3	0.688
	60	0.1	1.425
	120	0.3	0.022
	120	0.1	0.451
Enhanced SN Ia	60	Obs.	0.024
	60	0.3	0.012
	60	0.1	0.003
	120	0.3	<0.001
	120	0.1	<0.001

SFE and ehanced SN Ia models, which were already disfavoued with the existing data (BF $\sim$ 0.002 and 0.02,respectively), become even more disfavoured when the number of stars or the measurement precision increases (BF $<$ 0.001). Similarly, the cnstant SFR model, which was marginally disfavoued by the existing observations (BF $\sim$ 0.2), becomes strongly disfavoued (BF $\sim$ 0.002) if the measurements precision is improved to $\lesssim$0.3 dex.

On the other hand, ruling out the linear-exponential SFR, metal-loading, longer SN Ia delay, and no SN Ia models remains challenging even with improved data sets due to the similarities in the MDFs they predict. In the case of the linear-exponential model, doubling the sample size has little effect on the model's BF, while increasing the precision results in only a marginal improvement in the model discrimination (BF $\sim$ 0.1). We find the opposite is true for the other three models; increasing the precision provides little extra discriminatory power, while doubling the sample size yields a minor reduction of the BF by a factor of $\sim$2–3, which is not enough to confidently rule them out. Discriminate between these models and the fiducial model from the MDF alone may theoretically be possible with an even larger sample of precise measurements, but given the distance to Eri II and its lack of bright stars, acquiring such a data set is infeasible for the foreseeable future. Instead, the validity of these alternative models is better evaluated through additional measurements (e.g. [α/Fe], observed metal-loading factors) or plausibility arguments (e.g. the number of expected SN Ia).

As a concluding remark, we note that increasing the sample size or measurement precision does not always result in a reduction of the BF for the alternative models due to the stochastic sampling of our mock data. For example, the BF of the metal-loading model with $N_{\rm star} = 60$ increases from 0.173 to 0.568 when the uncertainties are reduced from 0.3 to 0.1 dex. This serves as a cautionary example against over-interpreting BFs that are of $\mathcal{O}(1)$. As a rule of thumb, we suggest that a BF of $\lesssim$0.01 is necessary to confidently rule out a model.

This paper has been typeset from a TEX/LATEX file prepared by the author.